Cliff-top boulder morphodynamics on the high–energy volcanic rocky coast of the Reykjanes Peninsula (SW Iceland)

Ronan Autret, David Didier, Serge S. Suanez, Pierre Stéphan, Jérôme Ammann, Jérémy Baudry, Björn Erlingsson, Sigurður Sigurðarson

Marine Geology

Cliff-top boulder morphodynamics on the high–energy volcanic rocky coast of the Reykjanes Peninsula (SW Iceland)

--Manuscript Draft--

Manuscript Number:	MARGO-D-22-00270R1
Article Type:	VSI:Rock coast dynamics
Keywords:	boulder; cliff-top; storm; basaltic coast; survey; Iceland
Corresponding Author:	Serge Suanez, Professor Université de Bretagne Occidentale Plouzané, FRANCE
First Author:	Serge Suanez, Professor
Order of Authors:	Serge Suanez, Professor
	Ronan Autret, post-doc
	David Didier, Professor
	Pierre Stéphan, Researcher
	Jérôme Ammann, Ingineer
	Jérémy Baudry, Research assistant
	Björn Erlingsson, Research
	Sigurður Sigurðarson, Engineer
Abstract:	Cliff-top boulder deposits (CBDs) are morphological indicators of high-energy conditions. Since 2014, a monitoring of CBDs dynamics has been undertaken on the south-western coast of Iceland (Reykjanes Peninsula) to monitor their long-term activation (quarrying, transport and deposition) as a proxy of the inter-annual winter storminess variations and basaltic cliff erosion processes in a context of rocky coast progradation. Annual topomorphological surveys of four study sites were conducted and Structure-from-Motion photogrammetry was performed to quantify CBDs displacements. Hydrodynamic conditions were analyzed based on offshore waves and water level. Results show that CBDs activation occurs every winter, regardless of the variability of hydrodynamic conditions. Depending on the site and the year, more than 2% and 17% of the CBDs accumulated above 8 m to 10 m asl at the top of the cliffs are regularly mobilized. While inland movements represent the main mode of transport of blocks (between 50% to 60%), seaward and longshore movements are also well represented (10% to 20%). Longshore displacement is favored by the wide tabular morpho-structural setting of the wave-scour cliff-top platforms, which is explained by the structure of pāhoehoe lava flows. The activation of CBDs –measured from the volumes of displaced boulders–, shows a good correspondence with the frequency and duration of storms. However, as was the case during the winter of 2018-2019, it was rather the intensity of two highly morphogenic episodes combining storm waves and especially very high spring tide water levels, that generated the largest boulders displacements. Substantial interannual activation of the CBDs confirms that they constitute an important and still understudied proxy of the morphogenic system of high-energy rocky coasts, whose the dynamic in terms of carrying, transport, and deposition, could significantly increase with rising sea level.
Suggested Reviewers:	Raphaël Paris Raphael.Paris@uca.fr
	Ronadh Cox rcox@williams.edu
	Stéphane Costa stephane.costa@unicaen.fr
	Christophe Morhange morhange@cerege.fr

	Larissa Naylor Larissa.Naylor@glasgow.ac.uk
	Christine Authemayou christine.authemayou@univ-brest.fr
Response to Reviewers:	

Cliff-top boulder morphodynamics on the high–energy volcanic rocky coast of the Reykjanes Peninsula (SW Iceland)

Ronan Autret [1], David Didier [1,2], Serge Suanez [3*], Pierre Stéphan [4], Jérôme Ammann [5], Jérémy Baudry [6], Björn Erlingsson [7], Sigurður Sigurðarson [8]

[1]Laboratoire de Dynamique et de Gestion Intégrée des Zones Côtières, Chaire de Recherche en Géoscience Côtière, Université du Québec à Rimouski, Rimouski, QC G5L 3A1, Canada

[2]Northern and Arctic Coastal Research Lab, Center for northern studies, Québec-Océan, Université du Québec à Rimouski, Rimouski, QC G5L 3A1, Canada

[3]Université de Bretagne Occidentale, CNRS, UMR LETG 6554, rue Dumont d'Urville, Institut Universitaire Européen de la Mer, 29280 Plouzané, France

[4] CNRS, UMR LETG 6554, Institut Universitaire Européen de la Mer, rue Dumont d'Urville, 29280 Plouzané, France

[5] CNRS, UMR LGO 6538, Institut Universitaire Européen de la Mer, rue Dumont d'Urville, 29280 Plouzané, France

[6] Laboratoire de physique des océans, Institut des Sciences de la mer, Université du Québec à Rimouski, Rimouski, QC G5L 3A1, Canada

[7] University Centre of the Westfjords, Suðurgötu 12, 400 Isafjordur, Iceland

[8] Icelandic Road and Coastal Administration (IRCA) - Vegagerðin, Borgartúni 5-7, 105 Reykjavík, Iceland

[*]Corresponding author: Serge Suanez
E–mail adress: serge.suanez@univ-brest.fr

Abstract:

Cliff-top boulder deposits (CBDs) are morphological indicators of high-energy conditions. Since 2014, a monitoring of CBDs dynamics has been undertaken on the south-western coast of Iceland (Reykjanes Peninsula) to monitor their long-term activation (quarrying, transport and deposition) as a proxy of the inter-annual winter storminess variations and basaltic cliff erosion processes in a context of rocky coast progradation. Annual topomorphological surveys of four study sites were conducted and Structure-from-Motion photogrammetry was performed to quantify CBDs displacements. Hydrodynamic conditions were analyzed based on offshore waves and water level. Results show that CBDs activation occurs every winter, regardless of the variability of hydrodynamic conditions. Depending on the site and the year, more than 2% and 17% of the CBDs accumulated above 8 m to 10 m asl at the top of the cliffs are regularly mobilized. While inland movements represent the main mode of transport of blocks (between 50% to 60%), seaward and longshore movements are also well represented (10% to 20%). Longshore displacement is favored by the wide tabular morpho-structural setting of the wave-scour cliff-top platforms, which is explained by the structure of pāhoehoe lava flows. The activation of CBDs –measured from the volumes of displaced boulders–, shows a good correspondence with the frequency and duration of storms. However, as was the case during the winter of 2018-2019, it was rather the intensity of two highly morphogenic episodes combining storm waves and especially very high spring tide water levels, that generated the largest boulders displacements. Substantial interannual

activation of the CBDs confirms that they constitute an important and still understudied proxy of the morphogenic system of high-energy rocky coasts, whose the dynamic in terms of carrying, transport, and deposition, could significantly increase with rising sea level.

Keywords: boulder, cliff-top, storm, basaltic coast, survey, Iceland.

1. Introduction

Coastal boulder deposits (CBDs) are supratidal coarse-clastic sediments dislodged and transported by high-energy waves to the coast. They are widespread geomorphological features of high-energy rocky coasts such as the Atlantic coasts of western Europe (Williams and Hall, 2004; Hall et al., 2006; Suanez et al., 2009; Oliveira et al., 2020b; Cox et al., 2012) and NW Africa (Mhammdi et al., 2019), the Pacific coasts –including Tasman Sea coast–, of eastern Asia (Goto et al., 2011, Kennedy et al., 2016, 2017), and Australia and New-Zeland (Sussmilch, 1912; Bishop and Hughes, 1989; Shelley, 1968), or the coasts of remote oceanic islands fully exposed to powerful oceanic swells (Etienne and Paris, 2010; Richmond et al., 2011b). CBDs are also found on the coasts of semi-enclosed maritime basins exposed to intense meteorological disturbances such as along the Mediterranean coasts (Deguara and Gauci, 2017; Delle Rose et al., 2020; Pepe et al., 2018; Piscitelli et al., 2017; Scicchitano et al., 2020; Terry et al., 2016).

CBDs are probably one of the most controversial types of subaerial coastal deposits among coastal sedimentary assemblages (Etienne et al., 2011; Kennedy et al., 2021; Lau and Autret, 2020; Paris et al., 2011). Their topographic positions on supratidal cliff-top platforms can reach between 10 to 20 m above the high spring water level, up to 30 m in some cases, and weigh up to 620 tons for the most massive (Cox et al., 2018a). A large part of the dedicated literature on CBDs focuses on whether they are tsunami or storm deposits (Nott, 2003; Saintilan and Rogers, 2005; Williams and Hall, 2004; Switzer and Burston, 2010; Richmond et al., 2011a; Prizomwala et al., 2015; Kennedy et al., 2021). In recent years, numerous studies have demonstrated the critical involvement of giant storm waves in the quarrying, transport, and deposition processes of CBDs, through *(i)* their morphosedimentary characteristics (Cox et al., 2018b; Etienne and Paris, 2010; Foster et al., 1991; Goto et al., 2010; Nanayama et al., 2000), *(ii)* the surveys carried out before and after high-energy storm events (Autret et al., 2016a; Fichaut and Suanez, 2010, 2011; Goto et al., 2012; May et al., 2015; Richmond et al., 2011a; Spiske and Bahlburg, 2011; Cox et al., 2018a), *(iii)* the critical analysis of theoretical boulder transport equations based on hydrological forcing (Dewey and Ryan, 2017; Lau et al., 2016; Prizomwala et al., 2015; Salzmann and Green, 2012; Shah-Hosseini et al., 2016; Soria et al., 2018; Kennedy et al., 2017, 2021), and *(iv)* the modelling and/or laboratory experiments (Bressan et al., 2018; Cox et al., 2019; Hansom et al., 2008; Watanabe et al., 2019; Weiss and Sheremet, 2017; Zainali and Weiss, 2015; Kennedy et al., 2016).

Cliff-top boulder deposits are highly persistent landforms in coastal landscapes. They constitute sedimentary archives capable of providing essential information on past wave climates extreme nearshore wave events (Ávila et al., 2020; Oliveira et al., 2020a). This is a key issue for future research on coastal boulder deposits (Cox et al., 2019), but we still have limited knowledge on their preservation potential. Therefore, CBDs may be considered as relevant geological records in coastal environments especially from their genesis to the moment they are considered as inert deposits (Cooper et al., 2019; Spiske et al., 2019). As indicated by Cox et al. (2019), they represent an effective proxy for long-term storminess analysis. The high frequency monitoring of CBDs carrying, transport and deposition may provide valuable information on the significant long-term variations of meteo-oceanic conditions, especially for the winter storm-periods. Coastal monitoring on sandy coast has been conducted in many

multi-decade research programs across the world and has proven its effectiveness to build up knowledge on the functioning of coastal environments driven by regular storms (Turner et al., 2016; Jaud et al., 2019; Banno et al., 2020; Castelle et al., 2020; Bertin et al., 2022; Nicolae Lerma et al., 2022). Some experiments of CBD monitoring based on at least one annual measurement have been undertaken (Nagle-McNaughton and Cox, 2020), notably on the Brittany coast (Autret et al., 2018), but they remain very anecdotal compared to the monitoring carried out on sandy beaches.

In this paper, we present the first results of a topo-morphological monitoring of CBDs started in 2014 on the coast of the Reykjanes peninsula, located in SW Iceland. This paper aims to study the impact of winter storms on the erosion of basaltic cliffs, resulting in the accumulation of CBDs at their top. We present annual monitoring data between 2014 and 2019 from 4 study sites corresponding to rocky cliff areas where CBDs are accumulated. These data are then analyzed considering winter weather and ocean conditions, specifically swell and water levels. Through this work, the correspondence between winter forcing conditions and CBD activation is analyzed.

2. Study area

2.1 Geological and geomorphological settings

The study area corresponds to a low rocky-cliff (with cliff-top elevations between 4 and 15 m above mean sea level - asl) located on the south-western coast of the Reykjanes Peninsula, in the south-west of Iceland (Fig. 1). The Reykjanes Peninsula corresponds to the southern part of the Icelandic Western Volcanic Zone, which is the transition area between the Reykjanes Ridge to the West and the Western Rift zone to the East (Einarsson, 1991). In this area, the volcanic activity has been quasi-continuous since the Mid Pleistocene, with thirteen historic eruptions (post 1200 BP), and at least nine prehistoric eruptions (Einarsson et al., 1991; Einarsson and Jóhannesson, 1989; Jóhannesson, 1989; Jóhannesson and Einarsson, 1988b, 1988a; Jónsson, 1983); the last eruption in Fagradalsfjall started in March 2021. This geological setting attests that this SW part of Iceland was never glaciated during the cold phases of the Quaternary period, and that as such, the boulders (e.g. CBDs) accumulated at the top of the cliffs were not eroded nor deposited by the glacier ice processes. Therefore, the Reykjanes Peninsula is indeed an active prograding lava delta, which corresponds to a particular case among rocky coast types, showing exacerbated morphosedimentary dynamics as a result of strong hydro-morphosedimentary disequilibrium (Marie, 2007; Ramalho et al., 2013).

Etienne and Paris (2010), and Autret et al. (2016b) described the lithostructural setting of this Reykjanes Peninsula rocky coast, focusing on the diversity of CBDs accumulated along more than 30 km of coastline.

Fig. 1. Location map. (a) Regional map of the North-East Atlantic showing boxed inset location of map (b). (b) Zoom on the study area. Squares refer to the four study sites. The tide gauges and the wave buoy for observational datasets are displayed as black triangles and polygon, respectively. The polar plot shows the wave directions at the WW3 grid output from January 1948 to April 2018 (located at W22.5°; N63.5°, 35 km south of Grindavík, ~250 m depth). (c) and (d) show the monthly statistics of modeled significant wave height and peak period between 1948 and 2018, respectively. Bars indicate monthly averaged wave statistical parameters with the corresponding standard deviation (vertical error bars).

The stack of lava flows through time is a determining factor in the morphology of the cliffs, the coastline shape and the cliff-top boulder deposits. The cliff-top boulder deposits stand on supratidal platforms that always correspond to the structural surface of pāhoehoe lava flows (Fig. 2). Basaltic pāhoehoe is generally characterized by a smooth or folded continuous crust

without (or few) rough topographies (Gregg, 2017). Typically, the structure of pāhoehoe lava surface is caracterized by circular wrinkles which look like ropes and therefore is called ropy pāhoehoe. These surface features are due to the movement of very fluid lava under a congealing surface crust inducing a behavioral difference between the center and the top-skin of the lava flow. However, the surface texture of pāhoehoe surface varies widely with increasing distance from the lava source, displaying in some cases all kinds of major rough topographies of various shapes often referred to as lava sculpture (e.g., collapsed tumuli, unusual craters, craters with raised rims, lava ponds, lava-rise –inflation– pits, lava-rise, inflation plateaus, etc.) (Detay and Hróarsson, 2018).

In cross-section, the vertical structure of pāhoehoe flows presents 3 distinct zones (Aubele et al., 1988; Autret et al., 2016b; Gregg, 2017): (i) an upper crust, typically vesicular and glassy or microcrystalline; (ii) an interior massive zone; and (iii) a relatively thinner basal crust that is similar in morphology to the upper crust. The top of the upper vesicular zone is often a repetitive sequence of glassy and red or maroon scoria, or slab-like layers a few centimers thick, with fluid surface textures (Fig. 2). The erosion of this zone by waves provides sand, rubbles, pebbles-size particles which constitute the major part of the CTSD's accumulations. The central non-vesicular (dense) zone is characterized by distinct vertical columns consisting of clustered large vesicles with internal platy structures favoring the quarrying of large boulders by waves along the cliff sections. These few larger boulders are generally deposited front of the CTSD's accumulations (Fig. 2).

This lithostructural context exerts a strong control on the clast size at a local scale. Pieces of basalt columns coming from flow interiors form the largest boulders (typically, b-axis>50 cm). They sometimes break into smaller boulders, but most of the small boulders (b-axis<50 cm) are typically brought by the erosion of superficial and interflow zones. In some cases (see Katlahraun site in Fig. 3c), few collapsed and well-rounded boulders are also projected from the tidal zone of the base of the cliff to the cliff-top (Autret et al., 2016b) (Fig. 2).

Figure 2. Lithostructural setting of the basaltic coastal bedrock of the Reykjanestá Peninsula. (a) Selatangar site; (b) Katlahraun site; (c) Reykjanestá site.

The four study sites (Kerling, Reykjanestá, Katlahraun and Selatangar) are presented in Fig. 3. They are located on post-glacial basaltic outcrops aged from ~1900 to ~7000 BP resulting from subaerial volcanism (Sæmundsson et al., 2016). As indicated above, because of their ages and locations, these CBDs have a modern origin and are only related to high-energy wind-generated wave erosion processes (Etienne and Paris, 2010).

Kerling (Fig. 3a) is a rocky promontory facing west. It is part of the Kerling volcanic complex. The basaltic substratum is aged ~1900-~2400 BP. The site is composed of three main geomorphological units: *(i)* bluffs of 2 m to 4 m high and oriented N-S; *(ii)* a barren and rough supratidal platform of 2 m to 4 m elevations asl where a few very coarse boulders are trapped; *(iii)* a boulder ridge of 165 m long, 70 m wide and 3 m tall on average. The boulder ridge is oriented N-S and faces West at a minimum inland distance (D_{min}) of 20 m from the edge of the supratidal platform and a maximum inland distance (D_{max}) of 75 m from the cliff edge.

Reykjanestá (Fig. 3b) is the southwestern tip of the Reykjanes Peninsula, exposed South to SW. The basaltic substratum is older than ~2400 BP and younger than ~7000 BP. It also presents three main geomorphological units: (1) vertical cliffs of 4.5 m to 5 m high, oriented N-S in the west part and NW-SE in the south part; (2) a cliff-top platform at an average elevation of 4.8 m asl, barren and relatively smooth; (3) a boulder ridge located close to the cliff edge (D_{min} = 1 m, D_{max} = 14 m), oriented N-S, 85 m long, 25 m to 30 m wide and 2 m tall on average.

The cliff-top boulder deposits of Katlahraun (Fig. 3c) stands on a basaltic substratum aged ~1900-~2400 BP. The geomorphological setting of this site is more complex with two additional geomorphological units: (1) bluffs topped between 2 m and 3 m asl and oriented E-W; (2) an intermediate supratidal platform barren and moderately rough at an average elevation of 3 m asl; (3) steps separating the intermediate supratidal platform and the top platform (e.g., P2 and P3 in Fig. 3c). The top of this step is considered as the cliff-top edge of this site; (4) a top platform at an average elevation of 4 m asl, barren and relatively smooth; (5) a boulder ridge of 150 m long, 30 m width and 2 m tall on average. The boulder ridge is oriented E-W and faces South. It is located at distances ranging from 15 m to 30 m from the cliff edge.

Selatangar (Fig. 3d) is part of the same lava flow unit as Katlahraun (aged ~1900-~2400 BP). It also presents three main geomorphological units: (1) vertical cliffs of 5 m high, oriented NW-SE; (2) a cliff-top platform barren and relatively smooth at an average elevation of 8 m asl; (3) a boulder ridge located at distances ranging from 8 m to 30 m from the cliff-edge, oriented NW-SE, 200 m long, 20 m to 40 m wide and 2 m to 3 m tall on average.

Fig. 3. Presentation of the four study sites. Kerling (a), Reykjanestá (b), Katlahraun (c), Selatangar (d), showing for each site an oblique aerial photography, a detailed topography and a 2D view of surface profiles extracted from the DEMs.

2.2 Oceanographic settings

The Reykjanes Peninsula is located north of the North Atlantic storm track and therefore experiences frequent storm waves (Davies, 1972; Einarsson, 1976). The wave climate is characterized by a strong seasonal modulation of the monthly-averaged significant wave height (*Hs*), ranging from 1.5 m in July to 3.6 m in January. The four winter months (December to March) are particularly energetic with *Hs* reaching 3.5 m in December (σ =1.7 m), 3.6 m in January (σ =1.7 m), 3.6 m in February (σ =1.8 m) and 3.2 m in March (σ =1.7 m) (Fig. 1c). The significant wave height (*Hs*) frequently reaches 8 m during storms (Sigbjarnarson, 1986), with a probable maximum *Hs* of 16.7 m recorded by a buoy in January 1990 (Tomasson et al., 1997). As a result of the narrow continental shelf, wave energy poorly dissipates into nearshore waters. Ocean waves are a major driver of coastal change in Iceland, but the impacts of storms on coastal settlements (mostly overland flooding resulting from overwash and overtopping) have been clearly linked to the concurrent forcing during peak events, i.e., when peak storm waves coincide with high tides. For instance, damages observed on buildings, roads, and coastal structures during a major coastal flood on January 9, 1990, in Stokkseyri were among the most important ever observed in south Iceland since 1910 (Geirsdóttir et al., 2014). This event occurred under an extremely low-pressure system (928 hPa), contributing to an unusually high tide (above 4 m in Reykjavik in the bay of Faxaflói), and powerful waves reaching 23 m near Surtsey (Viggósson et al., 2016). In Grindavík, the tidal range is slightly lower (mean spring tide of 3.2 m compared to 3.8 m in Faxaflói) with a mean sea level of 1.88 m (Larusson, 2010). Finally, there is no sea ice formation in this area of Iceland because of the warmer water discharge from the Irminger current. Wave energy is not attenuated by coastal sea ice during the winter months. Sea ice brought by the East Greenland Current from the polar basin is also too scarce to bring significant protection against winter storms (Etienne and Paris, 2010).

3. Methods

We quantitatively investigated cliff-top boulders and boulder ridges' morphosedimentary dynamics on the four study sites. Field surveys started in 2014 and are still ongoing. In this paper, the data and surveys conducted over the period 2014-2019 are presented (Table 1). The field measurement campaigns were carried out once a year in spring (usually in

May) after the winter storm period. The measurements consisted of topomorphological surveys based on ground measurements and very high-resolution topographic monitoring using *Kite Aerial Photography* (KAP) and *Unmanned Aerial Vehicle* (UAV).

Table 1.
Inventory of the topomorphological surveys achieved between 2014 and 2019.

	Field campaign activities	Methods	Sites
2014, May 11 to 18	Field reconnaissance, identification of CBDs, block size measurements, morphological measurements and field photographs	GPS-RTK, decameters, cameras	30 km of coastline from Selatangar to Kerling
2015, May 4 to 15	Topo-morphological survey	KAP, GPS-RTK	Selatangar, Katlahraun, Reykjanestá, Kerling
2016, May 9 to 19	Topo-morphological survey	KAP, GPS-RTK	Selatangar, Katlahraun, Reykjanestá, Kerling
2017, May 14 to 24, and August 27 to September 3	Topo-morphological survey	KAP, UAV (Phantom2 - DJI®), GPS-RTK	Selatangar, Katlahraun, Reykjanestá, Kerling
2018, May 16 to 26	Topo-morphological survey	UAV (Phantom4 Pro - DJI®), GPS-RTK	Selatangar, Katlahraun, Reykjanestá, Kerling
2019, May 12 to 19	Topo-morphological survey	UAV (Phantom4 Pro - DJI®), GPS-RTK	Selatangar, Katlahraun, Reykjanestá

3.1 Low-altitude aerial imagery and topography

Low-altitude aerial surveys (using KAP and UAV) were carried out, providing a detailed orthorectified aerial imagery of the boulder deposition and mobility areas. Digital Elevation Models (DEM) were created with Structure -from-Motion and Multi-View Stereo (SfM-MVS) processing (Fonstad et al., 2013; Westoby et al., 2012; Nagle-McNaughton and Cox, 2020; Jaud et al., 2019) (Fig. 4).

The KAP surveys were performed in May 2015, 2016 and 2017 with the following settings (Table 1): (1) two kites were alternatively used as lifters, a Delta Trooper (Dan Leigh®) for strong winds and a HQ Kites® Flowform 4.0 for light winds; (2) aerial photographs were taken with a Ricoh® GR camera (16.2 MP resolution, fixed focal length of 28 mm in the 35 mm format) connected to the kite line by a BROOXES® Gent-X picavet set; (3) ground control points (GCPs) and ground validation points (GVPs) were surveyed by a Topcon Hyper V Differential GPS in Real Time Kinematics mode (Fig. 4). X, Y and Z coordinates were referenced to EPSG 3057 (ISN93). The same KAP settings or a UAV (DJI®, Phantom 2 and 4 Pro equipped with a 20 MP camera with an equivalent focal length of 24 mm and stabilized on the 3-axis) were used to collect aerial images in August 2017, May 2018 and May 2019 (note that there is no data for Kerling in 2019 due to bad weather). KAP images were collected at multiple angles and altitudes depending on weather conditions. The variability of the shooting angles and heights did not affect the final data quality. Drone images were collected at a constant altitude of ~50 m and angle of -88° (subnadir) with flight paths set up to provide 80% overlap between consecutive images and 70% sidelap between contiguous paths. These settings were selected according to previous studies' recommendations and performed very well (Dandois et al., 2015; Matthews, 2008; Mosbrucker et al., 2017; Torres-Sánchez et al., 2018).

Fig. 4. SfM-MVS methodological workflow. (a) Raw images are first collected by KAP or UAV with a high rate of overlap along parallel transects. Ground markers corresponding to control (GCP) and validation (GVP) points have previously been positioned and measured on the study area. (b) step by step framework from data collection to work files generation. (c) shows an example of a volumetric differential between two surveys in the white-dotted box shown on (a). The left panel shows a surface rendering, and the right panel shows the corresponding diagrams.

We used SfM-MVS algorithms to reconstruct the georeferenced dense point clouds and the orthorectified aerial images from the aerial images sets. For each survey, a set of about 200 to 300 images were processed separately. The resulting dense point clouds were classified using a Cloth Simulation Filter (Zhang et al., 2016) in order to remove the vegetation and the storm debris (especially driftwood and many fishing buoys and ropes). We then generated DSMs at a 3 cm resolution by an Inverse Distance Weighting interpolation with a power of 2 (in this way, known values (the generated points) have more weight and the interpolation is closer to the ground truth). The DSMs accuracy in X, Y and Z were estimated by calculating the RMSE from GVPs independent of the GCPs network; the margins of error are between 0.044 and 0.025 m.

3.2 Geomorphic changes

Once data collected and postprocessed, interannual cliff-top boulder displacements and related morphosedimentary dynamics were investigated in two steps: (1) by computing the digital elevation model of differences (DoDs) from one survey to another in order to quantify the overall geomorphic changes, and (2) by tracking the displaced boulders that we were able to identify with certainty in order investigate boulder transport.

The DoDs were computed using the quantitative differencing method originally implemented by Wheaton et al. (2009), which improves the way to consider the total uncertainty of several topographic surveys in the DoDs, including uncertainties in the topographic survey data, the propagated error into the DoD and the significance of DoD uncertainty. A vertical detection threshold was set to 10 centimeters, minimizing the volumetric computation errors associated with SfM photogrammetry for the reconstruction of rough 3D surfaces. Nevertheless, this underestimates the net changes and the volumes given hereafter should therefore be considered as an order of magnitude rather than exact values.

When it was possible, individual transported and recognizable boulders were tracked using GIS geospatial tools. According to the topographic changes highlighted by the DoDs and field or high-resolution orthomosaic validations, pre- and post-transport boulders positions were measured. For each transported boulder found into its new position, we measured: *(i)* the length of the *a*-, *b*- and *c*-axis (*A, B, C*); *(ii)* the pre- and post-transport location (start_x, start_y, start_z, end_x, end_y, end_z); *(iii)* the closest pre- and post-transport distance from the seaward edge of the supratidal platform (start_d, end_d). The direction and the length of transport were then computed (transport_length and transport_bearing, respectively). Finally, the *a*-, *b*- and *c*-axis measurements were used to estimate the volume of each boulder, from which 20% were subtracted before computing the mass. One-way analysis of variance (ANOVA) was used to compare groups of displaced boulders in terms of masses, elevation and distance. A post-hoc Tukey test was performed to identify group pairing discrepancies. However, as noted above, most of the boulder movements associated with the morphological changes in the boulder ridges and/or clusters as a whole, could not be measured because it was not possible to identify the start and/or end zone of the boulder movement.

3.3 Analysis of the meteo-oceanic conditions

3.3.1 Wave conditions and water levels during the survey period (2014-2019)

Hourly observed water levels covering the period between June 2014 and April 2019 have been retrieved from the tide gauge in Sandgerdi Harbor, ~25 km from the study area (Fig. 1b). This gauge was selected in order to overcome large data gaps at the Grindavik tide gauge

in 2017. Following Bernier and Thompson (2015), the water level have been decomposed into tidal components and surge residual using the Matlab tidal analysis package T_TIDE (Pawlowicz et al., 2002). Note that local effects induced by basin morphology and barometric effects (e.g., seiches) can impact the overall surge signal (Donn and Wolf, 1972). Therefore, it is expected that the surge signal recorded in Sandgerði Harbor may not represent accurately the conditions in Grindavík. For this reason, less emphasis has been laid on this aspect in the present study.

Hourly offshore wave characteristics between December 1995 and April 2019, including significant wave height (*Hs*) and average wave period (*Tz*) were provided by the *Icelandic Road and Coastal Administration* for the Grindavík buoy (63°48.80'N; 22°27.63'E; 62 m depth) (Fig. 5b). This 24-yrs continuous timeseries was used for the wave model validation (Fig. 5c). Only the 2014-2019 timeframe was used for the current analysis of hydrodynamic conditions related to morphological changes.

Storminess was analyzed using a Peak Over Threshold method (POT) with a two-step threshold. Considering the high-energy wave climate near the study sites, the 99th percentile of the modeled significant wave height time series was used as a primary threshold for the strongest storms. The start and end time of the storm have been set according to a lower up- and down-crossing of the 95th percentile of the *Hs* time series, following the storm definition of Masselink et al. (2015) applied on the southwest coast of England. Ensuring that these storm events are all independent (*Hs* maxima are separated by at least a 24h independence criterion), observed water levels (*WL*) both at each maximum and during the events were extracted using the Sandgerði gauge as the reference to still water level.

Fig. 5. Modelled (a) and observed (b) offshore significant wave height (*Hs*) between 1948 and 2019. The WW3 validation period covers the period between 1995 and 2017. Debiased modelled *Hs* are plotted against observations at the Grindavík buoy (c). Example of surge waves overtopping cliffs at Reykjanestá on May 19, 2018 under stormy but not extreme wave conditions (*Hs* = 4 m) (d).

Joint probability occurrence of storms was quantified with copulas for the available observations period (2011-2019) using the MhAST toolbox (Sadegh et al., 2018). A time series of pairs of interest of the two hazard drivers *Hs*/*WL* was constructed using the *Hs* and *WL* maxima during each storm. The joint time series is short (8 years) but can be useful to understand the combinations of variables that could trigger boulder movement during this period. Following Sklar's theorem (Nelsen, 2006), if F_H (*Hs*) and F_W (*WL*) are the marginal distributions of significant wave height (*Hs*) and water levels (*WL*), a copula *C* combining these two marginal distributions represents the joint distribution function following:

$$F(Hs, WL) = C\big(F_H(Hs), F_W(WL)\big) = C(u_1, u_2)$$

If marginal distributions are continuous, *C* is unique and the joint probability density function *c*() can become:

$$c(u_1, u_2) = \frac{\partial^2 C(u_1, u_2)}{\partial u_1, u_2}$$

MhAST is based on the Multivariate Copula Analysis Toolbox (MvCAT) (Sadegh et al., 2017) and ranks each copula performance based on Likelihood, Akaike Information Criterion (AIC), Bayesian Information Criterion (BIC), Nash-Sutcliffe Efficiency (NSE), and Root Mean Squared Error (RMSE).

3.3.2 Long-term assessment of the potential activation frequency (1948-2019)

Offshore wave statistical parameters from January 1948 to March 2017 were retrieved from a Wavewatch III regional model hindcast covering the North Atlantic Ocean (0°-80°W; 0°-70°N) at a 0.5° resolution, described and validated in Masselink et al. (2016), at location W22.5°; N63.5° (35 km south of Grindavík, ~250 m depth) (Fig. 5a). To validate the model results, simulated and measured *Hs* and *Tp* (*Tp* = 1.4 *Tz*) at the Grindavík buoy located 3 km south of Grindavík at 62 m depth (Fig. 1) were compared for the period covering December 1995 to March 2017 (the buoy time series extends up to April 2019 in Fig. 5b). Comparisons of modeled *Hs* (Hs_{model}) with measured data show an averaged bias of 0.5 m, a squared correlation coefficient (ρ^2) of 0.67, and a normalized root-mean square error of 0.34. Modeled *Hs* were then linearly corrected following $Hs_{\mathrm{deb}} = Hs_{model}/0.96\text{-}0.58$, resulting in a significantly lower bias (0.02 m for the validation period). No correction was applied to the wave period time series considering the bias under 0.2 s between simulated peak wave periods and observations during storm conditions (i.e., when Hs_{deb} >7.5 m).

To better contextualize the observed cliff-top boulders' morphodynamics between 2014 and 2019, we analyzed the periodicity of annual offshore wave statistics and storm activity in SW Iceland over the historical period (1948-2019). Linear regressions were first computed to verify the presence of trends using the square correlation coefficient ρ^2 at a 95% significance level. A wavelet analysis was performed using the Analytic Wavelet Transform toolbox in Matlab (Aguiar-Conraria and Soares, 2014). The Morlet wavelet function was applied (ω0 = 6) over the annual time series of storm occurrence and annual wave characteristics with a lower and upper period of 2 and 50 years (pad = 0).

4. Results

4.1 Morphological changes and boulder transport

Morphological changes were quantified by DoDs calculation using low-aerial topographic data surveyed between 2015 and 2019 (except for Kerling, not surveyed in 2019). Additional qualitative analysis was also based on the 2014 field reconnaissance. The results presented hereafter are expressed in cubic meters per site and per winter, and then expressed as the relative volume of the total volume of each cliff-top boulder accumulation (percentage per winter). Note that these values are orders of magnitude, not fully accurate values.

Between May 2015 and May 2016, ~522 m^3 of boulders were transported at Kerling (corresponding in proportion to ~2.3% of the total number of boulders), ~17 m^3 at Reykjanestá (~0.8%), ~68 m^3 at Katlahraun (~1.1%) and ~41m^3 at Selatangar (~0.5%). The volume of transported boulders was higher between 2016 and 2017 than the previous year, with ~1081 m^3 at Kerling (~4.8%), ~100 m^3 at Reykjanestá (~4.8%), ~153 m^3 at Katlahraun (~ 2.4%) and ~103 m^3 at Selatangar (~1.3%). Between 2017 and 2018, ~665 m^3 of boulders were transported at Kerling, ~54 m^3 at Reykjanestá, ~69 m^3 at Katlahraun and ~33 m^3 at Selatangar. This corresponds to ~3% of the total number of boulders in the boulder ridge at Kerling, ~2.6% at Reykjanestá, 1.1% at Katlahraun and 0.4% at Selatangar. Finally, the greatest changes occurred during the last monitoring period (2018-2019) with ~369 m^3 of moved boulders at Reykjanestá (~17.6%), ~354 m^3 at Katlahraun (~5.6%) and ~141 m^3 at Selatangar (~1.7%). (Fig. 6a and 6b).

The successive DEMs and orthophotos also helped to identify the start and end positions of n = 988 recognizable boulders from one survey to the next, hereafter referred to as transported boulders. Between 2015 and 2016, n = 123 boulders were transported (i.e., n = 31 at Kerling, n = 35 at Reykjanestá, n = 33 at Katlahraun, and n = 24 at Selatangar), n = 360 boulders between 2016 and 2017 (i.e., n = 115 at Kerling, n = 73 at Reykjanestá, n = 83 at

Katlahraun, and $n = 89$ at Selatangar), $n = 281$ boulders between 2017 and 2018 (i.e., $n = 83$ at Kerling, $n = 50$ at Reykjanestá, $n = 50$ at Katlahraun, $n = 98$ at Selatangar), and $n = 224$ boulders between 2018 and 2019 (i.e., $n = 39$ at Reykjanestá, $n = 108$ at Katlahraun, $n = 77$ at Selatangar). We consider the distance between these two positions as a marker of boulders' movement, but these vectors should not be interpreted as the true trajectories of the CDBs. Boulders can indeed experience multiple movements during the same winter period, especially if it is characterized by several storm events (Autret et al., 2016a).

Fig. 6. Summary of transported boulders at each site between 2015 and 2019 expressed in absolute volume (m^3) (a) and relative volume of the total accumulation (%) (b). Boulder mass (kg) (c), elevation above sea level (m) (d) and inland distance from the cliff-top before transport (m) (e) are also shown.

The mass, the elevation and the inland distance of the transported boulders are summarized in Fig. 6c and 6e. There is a statistically significant difference between mean transported boulder masses (mean = 1.47 tons, $\sigma = 2.66$ tons) between sites, with significantly heavier transported boulders at Kerling compared to the other sites (one-way ANOVA $p<0.001$; post hoc Tukey HSD tested significance at the $p<0.001$ level). The heaviest boulders were all moved at Kerling (i.e., 29 tons between 2017 and 2018, 24 tons between 2015 and 2016, 22 tons between 2016 and 2017), but regardless of the year, no significant interannual difference in averaged transported masses is observed at this site ($p>0.3$). Eastwards of Kerling, more variability in transported CBDs is observed. The movement of the heaviest, and statistically heavier boulders in average than other years ($p<0.001$), were recorded between 2016-2017 in Katlahraun or 2018-2019 in Selatangar and Reykjanestá.

In average, CBDs are found at 7.28 m asl ($\sigma = 1.97$ m) (Fig. 6d), but in contrast to boulder mass, the averaged elevation of the transported boulders shows a statistically significant difference between all sites (one-way ANOVA $p<0.001$; post hoc Tukey HSD tested significance at the $p<0.001$ level). This is due to major topographic variabilities between all sites. Moreover, interannual variability in transported CBDs elevations varies greatly from one site to another. While transported CBDs elevations between 2015 and 2019 remain similar at Selatangar ($p>0.19$), transported boulders between 2016-2017 and 2017-2018 were higher than between 2015-2016 at Kerling ($p<0.05$). Statistically, averaged transported boulder elevations were higher (and at similar elevations) between 2016-2017 and 2018-2019 at Reykjanestá. Compared to these two periods at this southernmost cliff, transported boulder elevations were significantly lower between 2015-2016 and 2017-2018 ($p<0.001$). At Katlahraun, CBDs have been moved at higher elevations between 2018-2019 ($p<0.001$), and similarly to Reykjanestá, the averaged elevation of the moved boulders increased between the first two years of the surveys, followed by a decrease between 2016-2017 and 2017-2018, while an increase in transported boulder elevations is observed during the last year.

At Kerling, Katlahraun, and Reykjanestá (at this later site, the averaged boulder distance relative to the cliff edge are significantly shorter than other sites ($p<0.001$)), boulders were moved from the supratidal platforms to the boulder fields (including the ridges). It was not the case at Selatangar, the higher site, where transport was more limited to the cliff-top platform and the face of the boulder ridges. The inland distance of the boulders before transport was of the same order of magnitudes between 2015 and 2019 at Selatangar and Kerling, except at Katlahraun and Reykjanestá where significant increases of ~41% ($p<0.001$) and ~20% ($p<0.05$) are observed, respectively, at the end of the monitoring period (Fig. 6e).

Fig. 7 summarizes the raw transport directions. A large directional spreading in transported boulders is observed, both on a single site during a single period but also between each period. A majority of boulders was transported inland, which is consistent with the theoretical direction of wave-generated flows to the coast (60.7% at Kerling, 59.4% at Reykjanestá, 59.2% at Katlahraun and 59.4% at Selatangar). Seaward (22.3% at Kerling, 24.4%

at Reykjanestá, 27% at Katlahraun and 25.7% at Selatangar) and longshore transports (17% at Kerling, 16.2% at Reykjanestá, 13.8% at Katlahraun and 14.9% at Selatangar) are less important, suggesting deviated or reflected flows just as competent (Fig. 8a).

There is a slight difference in mass –several tens of kilos for all sites– between the three transport directions (Fig. 8b). The same applies for the inland distance of the boulders before transport. Boulders transported seaward were generally located further inland than inland and longshore transported boulders (Fig. 8d). On the other hand, there is an inverse relationship between the length of transport and the normalized transport direction (Fig. 8d). Inland transport is longer than longshore transport by factors 1.5 to 3 depending on the site, and longshore transport is slightly longer than seaward transport.

Fig. 7. Boulder transport directions relative to their initial location along the cliff-top at each site (a to d) between 2015 and 2019. The bin color scale indicates boulder masses (in tons), and the blue/green background shades in the roses represent seaward and inland transport, respectively.

Fig. 8. Normalized CTSD transport orientation analysis between 2015 and 2019 (a). Panels (d) and (d) represent transported boulder mass (kg.), distances from cliff-top (m) and length of boulder transport (m) relative to their initial location (inland, longshore, seaward).

4.2 Storm analysis over the survey period (2014-2019)

The wave climate along the southwestern coast of Iceland follows a strong seasonal cycle punctuated by lows (summer) and highs (winter) (Fig. 9a and 9b). Between June 2014 and April 2019, the monthly averaged significant wave height (*Hs*) was 2.2 m (σ = 0.9 m) offshore Grindavík (monthly $Hs_{98\%}$ = 4 m), with a mean peak period of 10.3 s (σ = 1.1s). During winter months (Dec., Jan., Feb., March), the monthly–averaged values of *Hs* and *Tp* increases to 3.15 m (σ = 0.6 m) and 11.4 s (σ = 0.7 s), respectively. The highest *Hs* reached 11.4 m (*Tp* = 16.8 s) on March 16, 2015. March 2015 was one of the most energetic months with monthly averaged *Hs* reaching above 4m (monthly averaged *Tp* = 12.1 s), but globally mean *Hs* values have been slightly higher in February 2018 (4.1 m, *Tp* = 12.04 s). These two months were therefore characterized by waves reaching more than a meter above the maximum monthly–mean value observed during the winter of 2015-2016 (*Hs* = 3.1 m in March).

Fig. 9. Time series of corrected 6-hourly *Hs* modelled offshore Grindavík (a) (grey lines) and hourly observed *Hs* at the Grindavík buoy from 2014 to 2019 (b). Monthly moving averages of observed (green line) and modelled (blue line) are also shown in (a) and (b). Storms are detected when *Hs* > 99th percentile *Hs* (thick dashed black line, a-b). Their duration is proportionally illustrated with bubbles in panels (a) and (b), and is calculated as the time spent above the 95th percentile *Hs* (thin dashed black line) on either side of the peak storm. Water levels (*WL*) at Sandgerði (hourly) are shown in (c) for 2014-2019. *WL* at the peak *Hs* during each storm are plotted as diamond, whereas the most extreme concurrent event is indicated by circles at the maximum *WL* during each storm event. Residual surge is indicated as a blue line.

Using the 1% exceedance *Hs* as a critical threshold for storm occurrence ($Hs_{99\%}$ = 7.6 m) and the lower secondary threshold $Hs_{95\%}$ as the trigger and end time of each event, observations show a total of 85 storms in southwest Iceland, offshore Grindavík, between December 1994 and May 2019. These storms (~3.5 storms per year) lasted 28h on average with mean significant wave heights (*Hs*) of 6.9 m ±0.7m. During the survey period (2014-2019), 22 distinct storms have been detected (~4.4 storms per year). Averaging 31 hours ±18h and lasting at least 17h, these events therefore lasted more than a tidal cycle and potentially had varying coastal impact intensities over the course of up to ~4 consecutive days (e.g., March 5, 2015). Most storms (8 events) occurred in winter 2014-2015 with a mean duration of 36 hours (mean *Hs* = 7.1 m and *Tp* = 14.2 s, mean peak *Hs* = 9.3 m and *Tp* = 16.7 s) (Table 2). Unfortunately, no detailed topographic measurements were carried out in 2014 and therefore we cannot

quantitatively address the morphogenic impacts of the 2014-2015 winter storms on the boulder activation. In winter 2015-2016, 3 storms occurred under slightly less energetic conditions (mean peak *Hs* = 8.7 m and *Tp* = 15.7 s). Earlier events are observed in the following storm seasons. A total of 6 storms occurred between October 2016 and February 2017 with similar storm characteristics (mean peak *Hs* = 8.3 m and peak *Tp* = 15.5 s). Only 3 storms impacted the coast in winter 2017-2018 (mean peak *Hs* = 8.8 m and *Tp* = 15.9 s). The following period (2018-2019), the only 2 storms recorded peaked at low tide (<–0.8 m), even though a particularly high tide (2.2 m) occurred during the February event.

Table 2
Storm characteristics during the survey period (2014–2019) on the southwest coast of the Reykjanes peninsula. Wave statistics (*Hs* and *Tp*) are derived from offshore observations at the Grindavík buoy. Observed water levels (referenced to mean sea level) were acquired at the Sandgerði tide gauge.

Storm #	date/time at peak event	Max. *Hs* (m)	Max. *Tp* (s)	Mean *Hs* (m)	Mean *Tp* (s)	Duration (h)	Water level (m)	Max. water level (m)	Time interval between peak storm and max. water level (h)
1	2014–12–09 12:00	7.9	18.5	6.9	14.9	25	-0.9	1.6	8
2	2015–01–08 09:00	8.4	17.2	6.8	14.1	48	1.4	1.8	1
3	2015–01–19 09:00	9.3	15.9	6.9	13.8	32	-0.2	1.9	21
4	2015–02–18 16:00	9.2	16.8	7.1	14.2	19	0.6	1.7	2
5	2015–03–05 07:00	8.6	16.7	6.5	14.0	94	1.5	1.7	1
6	2015–03–10 21:00	9.1	15.3	6.8	14.1	25	1.7	1.7	0
7	2015–03–14 11:00	10.7	16.3	7.8	14.3	35	0.9	1.0	11.5
8	2015–03–16 08:00	11.4	17.1	8.1	14.5	20	-0.7	1.2	5
9	2015–12–31 09:00	7.9	15.5	6.3	14.0	26	1.1	1.3	0.5
10	2016–03–12 14:00	8.5	15.5	7.0	13.1	17	-1.9	1.9	6
11	2016–03–14 02:00	9.5	16.0	7.2	14.6	23	-0.9	1.7	4
12	2016–10–03 14:00	7.8	16.0	6.3	13.9	28	-1.4	1.8	7
13	2016–10–20 01:00	8.6	15.1	6.6	13.3	31	-1.0	1.9	8
14	2016–12–13 19:00	8.8	15.4	6.4	13.4	19	1.4	2.1	11
15	2016–12–27 20:00	8.7	15.6	7.3	13.9	46	0.3	1.7	10
16	2017–01–21 00:00	7.5	14.0	6.4	12.7	20	0.7	0.8	2
17	2017–02–07 07:00	8.4	16.7	6.8	13.3	66	-0.4	1.6	46
18	2017–11–05 20:00	8.2	14.9	6.5	13.4	29	1.9	2.2	11
19	2018–01–09 13:00	9.0	15.7	6.9	14.0	21	1.0	1.4	1
20	2018–02–24 07:00	9.2	17.0	7.6	13.9	28	-0.7	1.2	7
21	2018-12-11 16:00	7,6	13.5	6,5	13	21	-0.8	1.3	8
22	2019-02-22 01:00	9,2	16.6	7,6	15	18	-1.7	2.2	7

A statistical analysis based on the joint occurrence of storms –defined as energetic wave events–, and water levels at Sandgerði was conducted to determine favorable conditions associated to extreme water levels capable of overtopping the cliff top. During the joint time series of storm events (2011-2019), 34 storms have been detected. Maximal tidal range during spring tides is ~4.5 m to 5 m. The maximum surge level recorded is about 0.66 m (99% surge = 0.21 m). Peak water levels reached the 99th percentile value (99% *WL* = 1.81 m) at least during one storm each year since January 2015, but the timing of the storm peak was not always synchronized with a high tide level (Table 2). Most peak storms occurred within ±6 hours of the highest water level (53%), and about 21% of events occurred within ±1h. In the last decade,

critical extreme combination of both high *Hs* and high water levels at the same time occurred only once, on March 10, 2015 (Fig. 9c).

Multivariate analysis and copulas were used to calculate the joint probability of *Hs* and water levels. Despite the short duration of the joint time series (8 years) –and acknowledging that copula model parameters depends on the length of observations (Sadegh et al., 2018)–, the best copula (Fig. 10a) describing the correlation structure between the peak storm (max *Hs*) and the highest water level is the Raftery copula (RMSE = 0.1098) (Nelsen, 2006). Fig. 10a shows the absence of correlation between both variables, but the joint probability contours indicate some variability in storm events characteristics. For values of *Hs* slightly above the detection threshold (7.5-8 m), joint probability contours are nearly vertical, indicating that these storm wave conditions can be observed under varying water levels. Moreover, storms during which water levels overpass the 99th percentile (1.82 m) are not uncommon, and they are mostly associated with $Hs \lesssim 9.5$ m. With increasing significant wave height above 9.5 m, lower rates of increases in joint probability (larger gaps between isolines) are associated with a lower variability in water levels (e.g., for a joint density probability of 0.8, storms associated with $Hs > 9.5$ m would occur above the 99th percentile of *WL*). Therefore, different configurations of events (*Hs*/*WL*) can have similar non-exceedance probability. For instance, a storm with high waves combined with low water levels (e.g., storm #11) can have a similar probability of occurrence than a less energetic storm event with almost twice the water level (e.g., storm #18). It is interesting to note that the last storm recorded, with $Hs = 9.2$ m and $WL = 2.2$m, has the highest joint probability ($p = 0.74$).

These results show that extreme events can yield the same return period (here shown in probability space only) while potentially inducing different morphogenic impacts on the coast. Despite the displacement of a significant volume of boulders during the survey period, the storms and the wave climate observed during the 2014-2019 period were not extreme compared to the whole storm history along the southwestern coast of Reykjanes Peninsula since 1948 (Fig. 10b). Storms with energetic waves ($Hs > 10$ m) lasted up to about a week (e.g., in January 1993 and 2002). Major coastal hazards have been observed under shorter but more intense storms (storm duration <3 days and $Hs > 12$ m) in 1990 and 1967 (Fig. 10b), during which coastal floods, damaged ships and also moving boulders have been observed (Geirsdóttir et al., 2014).

Fig. 10. The Raftery copula (a) shows the bivariate dependence structure of maximum significant wave height (*Hs*) and highest water levels observed during a single storm in southwest Iceland between 2011 and 2019. The copula isolines in (a) are plotted over data space, and all points represent observations. In (b), the density plot shows the duration (hours) and max. *Hs* of each detected storms between 1948 and 2019. Two of the most extreme storms in southwest Iceland during this period (Geirsdóttir et al., 2014) are indicated by dark dots (storms of 1967 and 1990). Green dots and colored diamonds represent the storms detected between 2014 and 2019. Diamonds (a) and (b) show the storms with the highest *Hs* observed in each season during the survey period (2014-2019). The colorbar represents point density in (b).

4.3 Long-term storm events analysis (1948-2019)

Between 1948 and 2019, there has been important variability both in terms of storm occurrence and storm duration offshore Grindavík. No storm occurred in 2007 and 2009, while the highest number of storms occurred in 1993 with 11 storms cumulating over ~22 days, followed by 1962 (9 storms, ~19 days) and 2015 (8 storms, ~13 days) (Fig. 11). Linear regression performed on both the total number of storms and cumulative days of storms annually do not show any trend ($R^2 < 0.02$) (Fig. 11a and 11b). However, the storm behavior exhibits a strong periodicity, as shown by the 3–year averages in Fig. 11a and 11b. Years with 3 storms or less occurred about 48% of the time but some periods with more, longer storms annually can be identified, such as between 1987 and 1995. Significant wave heights (*Hs*)

during storms also exhibits no particular trend (Fig. 11c), and similarly to the storm behavior, rather appears to have undergone periods of lows and highs. Overall, Fig. 11 clearly shows that the monitoring carried out in this study (2014-2019) were not done during the most energetic period, but rather in a period of diminishing storm occurrence and duration.

Fig. 11. Storm characteristics between 1948 and 2019 offshore Grindavík. The annual total number of storms (a) and duration (in days) (b) are shown with a 3-points moving average (solid lines). The linear regressions are plotted as dashed lines in panels (a) to (c). Wave characteristics during storms are shown in (c): mean *Hs*, mean peak *Hs* and maximum *Hs* during storms over a year are shown by khaki, green, and blue solid lines, respectively (circles represent the values in 2008).

The wavelet spectral analysis performed on the total storm duration (cumulative days over a year), mean storm duration and 99.8th percentile of *Hs* allows a more in-depth understanding of the storm variability, periodicity and transient dynamics over time. The wavelet power spectrums (left panels on Fig. 12a to 12c) show the frequency domain (*y* axis in period cycles) and the time dimension with areas of higher (pink) and lower (blue) power. The average spectral power exhibits a strong peak between 2 and 5 years for all three variables. This indicates that storm climate alternates between periods characterized by longer storms associated with more extreme wave heights, and somewhat calm periods with shorter storms on a timescale of 2 to 5 years. The alternating presence of warmer areas in the wavelet power spectrum (left panels on Fig. 12a to 12c) roughly between 1950 and 1965, 1975 and 1990, and 2005 and 2015 (>95% significant) also suggests that this periodicity is not stationary, which implies that the storm climate also alternates between periods of stability and periods of strong variability on a timescale of about 10 to 15 years.

Figure 12. Wavelet power spectrums (scalograms on the left) and averaged wavelet power over each frequency (right column), for the total number of days of storms (a), the mean storm duration annually (b) and the extreme wave height annually (99.8th percentile *Hs*) (c). The color bars on the right of the scalograms indicate power intensity. Black contours on the scalograms indicate the 5% and 10% significance levels, and the black vertical curves indicate the border of the cone of influence.

5. Discussion

5.1 Temporal frequency of cliff-top boulders movements in SW Iceland

The first finding of this 6-years monitoring is that cliff-top boulders were annually and substantially reworked. In comparison, between 2012 and 2017, pluriannual cliff-top boulder activation in Brittany was very limited, with no boulder displacements for certain years (Autret et al., 2018). In SW Iceland since 2014, hydrodynamic processes inducing wave overtopping the cliffs occurred each year on every study sites. These processes are usually described to be related to extreme storm wave events (Bressan et al., 2018; Hansom et al., 2008; Kennedy et al., 2017; Watanabe et al., 2019), generally combined with high spring tide in a macrotidal environment (Fichaut and Suanez, 2011; Autret et al., 2016a, Cox et al., 2018a). In the case of SW Iceland, such extreme meteo-oceanic conditions are not required to generate boulder displacements at the top of the cliffs. Indeed, the long-term analysis of morphogenic events combining extreme storm waves and high tide levels, showed that the 2014-2019 period was rather less impacted compared to other years, such as winter 1990 and 1967. Only one event that perfectly paired extreme waves and high spring tide levels was observed in November 5, 2017 (storm #18). In details, our results highlight a significant interannual variability in boulder movement is observed. While in 2015-2016, 2016-2017, and 2017-2018, there is a good correspondence between storm frequency/duration (Fig. 9b), and the global volume of boulder displacements at each site (Fig. 6a and 6b), this is not the case for the winter of 2018-2019.

During this period, there was only one storm inventoried in February with high spring tide (Fig. 10a), while the volumes of displaced boulders were larger over the entire survey period (Fig. 6). In this case, it is not the frequency of winter storms that seems to have been the determining parameter for the movement of the boulders, but the intensity of an extreme event combining energetic waves and very high spring tide levels. Therefore, the interannual variability in boulder activation, or the correspondence between the morphogenic events frequency/intensity (i.e., occurrence of joint events combining storm wave and high spring tide level) and the volume of displaced boulders, would need more detailed analysis of nearshore and coastal hydrodynamic processes. As it stands, this monitoring based on annual survey does not allow us to answer this question, which also refers to the question of storm wave thresholds (Almeida et al., 2012; Grieco and DeGaetano, 2019), the efficiency of processes combining storm waves and a spring tide (Harley, 2017), or the impact of repeated low-energy storms *vs*. a single extreme storm event (Ferreira, 2005). As seen on Fig. 3c, cliff overtopping can occur with 4 m-high waves. Increasing the monitoring frequency of CBDs to a monthly basis, or even at the event scale, would help to better understand the various hydrodynamic conditions that generate boulder movement.

In addition, this survey shows that the interannual displacements of boulders at the four monitored sites show the same morphological signature both in terms of the total volume of boulders displaced, as well as in terms of the volume as a percentage of the global volume of the ridges (Fig. 6a and 6b). We can also note that globally, the mass of the transported boulders, as well as the altitude and the inland distance of these displacements, is proportionally the same for the four sites from year to year of monitoring (despite the lack of data for the Kerling site in 2018-2019) (Fig. 6c to 6e).

Globally, these results confirm the extremely stormy and morphogenic context of the meteo-oceanic forcing that impacts SW Iceland at these sub-polar latitudes. This is consistent with the fact that this coast faces the most energetic wave climate in the North Atlantic Basin (Betts et al. 2004; Ardhuin et al., 2019). Indeed, based on atmospheric condition analysis between 1931 and 1991, Schinke (1993) showed this zone of the north Atlantic basin (up to 60°-65° latitude) was 5 times more impacted by deep cyclones (≤990 hPa) than temperate latitudes (45°-50° latitude).

5.2 Specifities of the boulder displacements in Reykjanes Peninsula

A prominent characteristic of the cliff-top boulder deposits in the four study sites is their abundance and disposition of swash-aligned elongated ridges in a context of backstopped plateforms (Autret et al., 2016b; Etienne and Paris, 2010). As indicated by many authors, this type of morphological setting concerns imbricated boulders subject to frequent activation (Chen et al., 2011; Cox et al., 2012; Etienne and Paris, 2010; Lorang, 2011) which is in agreement with the results obtained by our surveys. We also indicated that the cliff-top boulder deposits of the Reykjanes Peninsula experience significant changes over small areas (few square meters) spread over the seaward side of the ridges without apparent pattern of mobility. Some coarse boulders (>10 tons and up to 29 tons during our monitoring) are moved while adjacent finer boulders (<1 ton) are unaffected.

The main dominant boulder transport direction (>50% of boulders displaced whatever the site and whatever the year) (Fig. 6) is oriented inland. This is in accordance with the fact that inland-directed transport is generally the most common for boulder displacements due to the cross-shore dynamic of storm wave facing cliffs. A significant part of the cliff-top boulders is transported toward the sea (22% to 27% of the transported boulders, depending on the site) and may be attributed to backwash processes. As shown by Cox et al. (2019), even if inland transport is always dominant, seaward boulder transport by backwash also occurred on the

context of backstopped platforms where boulder accumulations take the form of strongly fixed imbricated linear ridges. In that context, the energetic bore overtopping the cliff is reflected by the boulder ridge.

Longshore boulder transports are also observed on our studied sites as shown in Fig. 6 (between 10% and 30% of the displacements depending on the site and the year). This is mainly due to the oblique direction of the swell at break-up in relation to the orientation of the cliff edge characterized by a certain angle to the coastline. However, these movements are facilitated by the litho-morphostructural context of the wave-scour cliff-top platforms which are particularly tabular (Autret et al., 2016b; Etienne and Paris, 2010). This morphology is explained by the surface characteristics of pāhoehoe lava flows whose high fluidity produces smooth and flat surfaces as the lava solidifies (Fig. 2). In contrast, on the very chaotic and rough granite wave-scour cliff-top platforms of the old folded and fractured Armorican Hercynian massif (e.g., Banneg Island in Brittany), the longitudinal transport of boulders is made very difficult by the presence of multiple trapping microforms (i.e., steps, gullies, diaclases, hollow faults, etc.) (Fichaut and Suanez, 2011; Autret et al., 2016a).

5.3 Boulder activation as a proxy of long-term morphogenetic/catastrophic event analysis

The cliff-top boulders, throught the processes of their activation/displacement, appears to be an excellent proxy for the study of extreme events in terms of frequency and intensity. Systematic monitoring is crucial to study their morphodynamics. In addition to the proxy as geological archive they represent, it is also essential to better consider their movements and geomorphic interactions in the global high-energy rocky coast system. As shown for other coastal boulder deposits, repeated boulder activation is an important factor in platforms erosion (Cullen et al., 2018; Cullen and Bourke, 2018; Etienne, 2007; McKenna, 1990; Swirad et al., 2019; Naylor and Stephenson, 2010; Naylor et al., 2016). From a geomorphological perspective, further theoretical and field-based developments coupled to continuous boulder transport and hydrodynamic observations in their natural contexts are needed to help modelers to adapt existing morphodynamic models –or develop new ones– to cliff-top boulders transport and related morphological changes. From a coastal risk perspective, they are often used as a marker of inundation extents. But when activated, they also are a risk factor on its own. For instance, coastal hazards in southwest Iceland have clearly been associated to concomitant high waves and high water levels, and the timing of the peak storm (in terms of wave energy), spring tide and surge is considered as an important risk to coastal population (Geirsdóttir et al., 2014). Such extreme event can activate boulder movement or man-made CBDs-like structure (such as breakwaters) and turn them into projectiles against infrastructure. For instance, the 1990 flood event in Stokkseryri (67 km east of Grindavík), which occured at the highest tide level, is deeply rooted in the collective memory, especially because of the large rocks that were plucked from the breakwater and spread around the village. A similar event happened during storm Dennis (February 11 to 18, 2020) on the coast of Reykjanesbær, 19 km north of our study area (Fig. 13).

Figure 13. Boulder displacements during the storm event Dennis (14-15 February, 2020) in Reykjanesbær.

6. Conclusion

The southwest coast of Iceland, especially the Reykjanes Peninsula characterized by basaltic rocky-cliffs, is subject to an intense annual storm activity because it is located in the main track of the rail of winter atmospheric low-pressure systems that circulate in the Northern Atlantic basin. The monitoring that has been undertaken since 2014 shows that the CBDs accumulated

at the top of the cliffs are an excellent proxy to analyze the variability of this North-Atlantic cyclogenesis. However, the annual frequency of the survey does not allow us to study morphogenic processes on an episode scale; it nevertheless shows a good correspondence between the volumes of CBDs displaced and the frequency and/or intensity of storms over the entire winter period. In the longer term, this monitoring will also allow to evaluate the impact of storms on the coastal morphological dynamics of rocky coasts in a context of very high meteo-oceanic energy. In a context of climate change and the implications that this has on the modification of hydrodynamic conditions, particularly at lower temperate latitudes, this work is of great interest.

Acknowledgements

This research was supported by the "*Laboratoire d'Excellence*" LabexMER (ANR-10-LABX-0019), the ISblue project, Interdisciplinary graduate school for the blue planet (ANR-17-EURE-0015), and co-funded by a grant from the French government under the program "*Investissements d'Avenir*", and the region of Brittany, for the period 2014-2018. It was also funded by the "*Institut Paul Emile Victor*" (IPEV - French Polar Institut) through the research program EXTREMEVENT (Arctic - Project number 1216) for the period (2019-2022). Funding was also provided by the *Chaire de Recherche en Géoscience Côtière* and the *Fonds de recherche du Québec – Nature et technologies* (Postdoc Grant, Université du Québec à Rimouski). Research support was provided by Didier's NSERC Discovery Grant and Québec-Océan. We also acknowledge the help from Magnus H. Steinarsson from the *Icelandic Meteorological Office* (Veðurstofa Íslands) and Ingunn Erna Jónsdóttir from the *Icelandic Road and Coastal Administration* (Vegagerðin). We also thank Peter Weiss and Björn Erlingsson from the University Centre of Westfjords (Ísafjörður) for providing data and logistic help. We also acknowledge the help of Björk Sverrisdottir and Magnùs for their kindness and the always very warm welcome in Grindavík.

References

Aguiar□Conraria, L., Soares, M.J. 2014. The Continuous Wavelet Transform: Moving Beyond Uni- and Bivariate Analysis. *Journal of Economic Surveys*, 28, 344–375. https://doi.org/10.1111/joes.12012

Almeida, L.P., Vousdoukas, M.V., Ferreira, Ó., Rodrigues, B.A., Matias, A. 2012. Thresholds for storm impacts on an exposed sandy coastal area in southern Portugal. *Geomorphology*, 143–144, 3–12. https://doi.org/10.1016/j.geomorph.2011.04.047

Ardhuin, F., Stopa, J.E, Chapron, B., Collard, F., Husson, R., Jensen, R.E., Johannessen, J., Mouche, A., Passaro, M., Quartly, G.D., Swail, V., Young, I. 2019. Observing sea states. *Frontiers in Marine Science,* 6(124). https://doi.org/10.3389/fmars.2019.00124

Aubele, J.C., Crumpler, L.S., Elston W. E. 1988. Vesicle zonation and vertical structure of basalt flows. *Journal of Volcanology and Geothermal Research,* 35(4), 349–374. https://doi.org/10.1016/0377-0273(88)90028-5.

Autret, R., Dodet, G., Fichaut, B., Suanez, S., David, L., Leckler, F., Ardhuin, F., Ammann, J., Grandjean, P., Allemand, P., Filipot, J.-F. 2016a. A comprehensive hydro-geomorphic study of

cliff-top storm deposits on Banneg Island during winter 2013–2014. *Marine Geology,* 382, 37–55. https://doi.org/10.1016/j.margeo.2016.09.014

Autret, R., Suanez, S., Fichaut, B., Etienne, S. 2016b. Elaboration d'une typologie des dépôts de blocs supratidaux de sommets de falaise de la péninsule de Reykjanes (Islande). *Géomorphologie : relief, processus, environnement*, 22(1) , 61–76. https://doi.org/10.4000/geomorphologie.11272

Autret, R., Dodet, G., Suanez, S., Roudaut, G., Fichaut, B. 2018. Long–term variability of supratidal coastal boulder activation in Brittany (France). *Geomorphology,* 304 , 184–200. https://doi.org/10.1016/j.geomorph.2017.12.028

Ávila, S.P., Johnson, M.E., Rebelo, A.C., Baptista, L., Melo, C.S. 2020. Comparison of Modern and Pleistocene (MIS 5e) Coastal Boulder Deposits from Santa Maria Island (Azores Archipelago, NE Atlantic Ocean). *Journal of Marine Science and Engineering,* 8(6), 386. https://doi.org/ 10.3390/jmse8060386

Banno, M., Nakamura, S., Kosako, T., Nakagawa, Y., Yanagishima, S., Kuriyama, Y. 2020. Long-Term Observations of Beach Variability at Hasaki, Japan. *Journal of Marine Science and Engineering,* 8(11), 871. https://doi.org/10.3390/jmse8110871

Bernier, N.B., Thompson, K.R. 2015. Deterministic and ensemble storm surge prediction for Atlantic Canada with lead times of hours to ten days. *Ocean Modelling,* 86, 114–127. https://doi.org/10.1016/j.ocemod.2014.12.002

Bertin, S., Floc'h, F., Le Dantec ,N., Jaud, M., Cancouët, R., Franzetti, M., Cuq, V., Prunier, C., Ammann, J., Augereau, E., Lamarche, S., Belleney, D., Rouan, M., David, L., Deschamps, A., Delacourt, C., Suanez, S. 2022. A long-term dataset of topography and nearshore bathymetry at the macrotidal pocket beach of Porsmilin, France. *Scientific Data*, 9(79). https://doi.org/10.1038/s41597-022-01170-3

Betts, N.L., Orford, J.D., White, D., Graham, C.J. 2004. Storminess and surges in the south-western approaches of the eastern North Atlantic: the synoptic climatology of recent extreme coastal storms. *Marine Geology*, 210(1-4): 227–246. https://doi.org/10.1016/j.margeo.2004.05.010

Bishop P., Hughes M. 1989. Imbricate and fitted fabrics in coastal boulder deposits on the Australian east coast. *Geology,* 17(6), 544–547. https://doi.org/10.1130/0091-7613(1989)017<0544:IAFFIC>2.3.CO;2

Bressan, L., Guerrero, M., Antonini, A., Petruzzelli, V., Archetti, R., Lamberti, A., Tinti, S. 2018. A laboratory experiment on the incipient motion of boulders by high-energy coastal flows. *Earth Surface Processes and Landforms*, 43, 2935–2947. https://doi.org/10.1002/esp.4461

Castelle, B., Bujan, S., Marieu, V., Ferreira, S. 2020. 16 years of topographic surveys of rip-channelled high-energy meso-macrotidal sandy beach. *Scientific Data,* 7, 410. https://doi.org/10.1038/s41597-020-00750-5

Chen B., Chen Z., Stephenson W., Finlayson B.. 2011. Morphodynamics of a boulder beach, Putuo Island, SE China coast: The role of storms and typhoon. *Marine Geology*, 283, 106–115. https://doi.org/10.1016/j.margeo.2010.10.004

Cooper, J.A.G., Green, A.N., Vital, H., Lima-Filho, F.P. 2019. Geomorphology and clast assemblages of intertidal beachrock: Implications for submerged shoreline preservation. *Geomorphology,* 343, 106–118. https://doi.org/10.1016/j.geomorph.2019.07.003

Cox, R., Jahn K.L., Watkins, O.G., Cox, P. 2018a. Extraordinary boulder transport by storm waves (west of Ireland, winter 2013–2014), and criteria for analysing coastal boulder deposits. *Earth-Science Reviews*, 177, 623–636. https://doi.org/10.1016/j.earscirev.2017.12.014

Cox, R., Lopes, W.A., Jahn, K.L.. 2018b. Quantitative roundness analysis of coastal boulder deposits. *Marine Geology*, 396**,** 114–141. https://doi.org/10.1016/j.margeo.2017.03.003

Cox, R., O'Boyle, L., Cytrynbaum, J. 2019. Imbricated Coastal Boulder Deposits are Formed by Storm Waves, and Can Preserve a Long-Term Storminess Record. *Scientific Reports*, 9, 1–12. https://doi.org/10.1038/s41598-019-47254-w

Cox, R., Zentner, D.B., Kirchner, B.J., Cook, M.S. 2012. Boulder Ridges on the Aran Islands (Ireland): Recent Movements Caused by Storm Waves, Not Tsunamis. *The Journal of Geology*, 120, 249–272. https://doi.org/10.1086/664787

Cullen, N.D., Bourke, M.C. 2018. Clast abrasion of a rock shore platform on the Atlantic coast of Ireland. *Earth Surface Processes and Landforms*, 43, 2627–2641. https://doi.org/10.1002/esp.4421

Cullen, N.D., Verma AK, Bourke MC. 2018. A comparison of structure from motion photogrammetry and the traversing micro-erosion meter for measuring erosion on shore platforms. *Earth Surface Dynamics*, 6, 1023–1039. https://doi.org/10.5194/esurf-6-1023-2018

Dandois, J.P., Olano M, Ellis EC. 2015. Optimal Altitude, Overlap, and Weather Conditions for Computer Vision UAV Estimates of Forest Structure. *Remote Sensing*, 7, 13895–13920. https://doi.org/10.3390/rs71013895

Davies, J.L. 1972. Geographical variation in coastal development . Oliver and Boyd, Edinburgh

Deguara, J.C., Gauci R. 2017. Evidence of extreme wave events from boulder deposits on the south-east coast of Malta (Central Mediterranean). *Natural Hazards,* 86, 543–568. https://doi.org/10.1007/s11069-016-2525-4

Delle Rose, M., Fidelibus C, Martano P, Orlanducci L. 2020. Storm-Induced Boulder Displacements: Inferences from Field Surveys and Hydrodynamic Equations. *Geosciences*, 10, 374. https://doi.org/10.3390/geosciences10090374

Detay, M., Hróarsson, B. 2018. Mise en place des pāhoehoe par tubes et tunnels de lave : concept et signatures volcano-géomorphologiques. *Géomorphologie : relief, processus, environnement,* 24(4), 365-388. https://doi.org/10.4000/geomorphologie.12557

Dewey, JF, Ryan PD. 2017. Storm, rogue wave, or tsunami origin for megaclast deposits in western Ireland and North Island, New Zealand? *Proceedings of the National Academy of Sciences*, 114, E10639–E10647. https://doi.org/10.1073/pnas.1713233114

Donn, W.L., Wolf DM. 1972a. Seiche and Water Level Fluctuations in Grindavik Harbor, Iceland. *Limnology and Oceanography*, 17, 639–643. https://doi.org/10.4319/lo.1972.17.4.0639

Einarsson, M.A. 1976. Veðurfar á Íslandi. Iðunn, 150 p.

Einarsson, P. 1991. Earthquakes and present-day tectonism in Iceland. *Tectonophysics,* 189, 261–279. https://doi.org/10.1016/0040-1951(91)90501-I

Einarsson, S., Jóhannesson, H. 1989. Aldur Arnarseturshrauns á Reykjanesskaga (Age of the Arnarseturshraun lava flow, Reykjanes peninsula, SW-Iceland). *Fjölrit Náttúrufraedistofnunar*, 8, 15 p. https://utgafa.ni.is/fjolrit/Fjolrit_08.pdf

Einarsson, S., Jóhannesson, H., Sveinbjörnsdóttir, A.E. 1991. Krísuvíkureldar. II. Kapelluhraun og gátan um aldur Hellnahrauns (The Krísuvík fires. I. Age of the Kapelluhraun andHellnahraun lava flows,Reykjanes peninsula, Southwest Iceland). *Jökull*, 41, 61–80.

Etienne, S. 2007. Les plates-formes d'érosion marine des littoraux volcaniques, in: Etienne S., Paris R. (Eds.), Les littoraux volcaniques: une approche environnementale. Edit. Presses Universitaires Blaise-Pascal, Clermont-Ferrand, pp. 37–55.

Etienne, S., Buckley, M., Paris, R., Nandasena, A.K., Clark, K., Strotz, L., Chagué-Goff, C., Goff, J., Richmond, B. 2011. The use of boulders for characterising past tsunamis: Lessons from the 2004 Indian Ocean and 2009 South Pacific tsunamis. *Earth-Science Reviews,* 107, 76–90. https://doi.org/10.1016/j.earscirev.2010.12.006

Etienne, S., Paris, R. 2010. Boulder accumulations related to storms on the south coast of the Reykjanes Peninsula (Iceland). *Geomorphology*, 114, 55–70. https://doi.org/10.1016/j.geomorph.2009.02.008

Ferreira, Ó., 2005. Storm Groups versus Extreme Single Storms: Predicted Erosion and Management Consequences. *Jouranl of Coastal Research*, SI42, 221–227. http://www.jstor.org/stable/25736987.

Fichaut, B., Suanez, S. 2010. Dynamiques d'arrachement, de transport et de dépôt de blocs cyclopéens par les tempêtes : le cas de la tempête du 10 mars 2008 sur l'île de Banneg (archipel de Molène, Finistère). *Norois*, 215, 33–58. https://doi.org/10.4000/norois.3224

Fichaut, B., Suanez, S. 2011. Quarrying, transport and deposition of cliff-top storm deposits during extreme events: Banneg Island, Brittany. *Marine Geology,* 283, 36–55. https://doi.org/10.1016/j.margeo.2010.11.003

Fonstad, M.A., Dietrich, J.T., Courville, B.C., Jensen, J.L., Carbonneau, P.E. 2013. Topographic structure from motion: a new development in photogrammetric measurement. *Earth Surface Processes and Landforms,* 38, 421–430. https://doi.org/10.1002/esp.3366

Foster, I.D.L., Albon, A.J., Bardell, K.M., Fletcher, J.L., Jardine, T.C., Mothers, R.J., Pritchard, M.A., Turner, S.E. 1991. High energy coastal sedimentary deposits; an evaluation of depositional processes in Southwest England. *Earth Surface Processes and Landforms*, 16, 341–356. https://doi.org/10.1002/esp.3290160407

Geirsdóttir, G.E., Gísladóttir, G., Jónsdóttir, Á. 2014. Coping with storm surges on the Icelandic south coast: A case study of the Stokkseyri village. *Ocean & Coastal Management,* 94, 44–55. https://doi.org/10.1016/j.ocecoaman.2013.09.013

Goto, K., Kawana, T., Imamura, F. 2010. Historical and geological evidence of boulders deposited by tsunamis, southern Ryukyu Islands, Japan. *Earth-Science Reviews*, 102, 77–99. https://doi.org/10.1016/j.earscirev.2010.06.005

Goto, K., Miyagi, K., Kawana, T., Takahashi, J., Imamura, F. 2011. Emplacement and movement of boulders by known storm waves — Field evidence from the Okinawa Islands, Japan. *Marine Geology*, 283, 66–78. https://doi.org/10.1016/j.margeo.2010.09.007

Goto, K., Sugawara, D., Ikema, S., Miyagi, T. 2012. Sedimentary processes associated with sand and boulder deposits formed by the 2011 Tohoku-oki tsunami at Sabusawa Island, Japan. *Sedimentary Geology*, 282, 188–198. https://doi.org/10.1016/j.sedgeo.2012.03.017

Gregg, T.K.P. 2017. Patterns and processes: Subaerial lava flow morphologies: A review. *Journal of Volcanology and Geothermal Research*, 342, 3-12. https://doi.org/10.1016/j.jvolgeores.2017.04.022.

Grieco, M.B., DeGaetano, A.T. 2019. A climatology of extreme wave height events impacting eastern Lake Ontario shorelines. *Theoretical and Applied Climatology,* 136, 543–552. https://doi.org/10.1007/s00704-018-2502-9

Hall, A.M., Hansom, J.D., Williams, D.M., Jarvis, J. 2006. Distribution, geomorphology and lithofacies of cliff-top storm deposits: Examples from the high-energy coasts of Scotland and Ireland. *Marine Geology,* 232, 131–155. https://doi.org/10.1016/j.margeo.2006.06.008

Hansom, J.D., Barltrop, N.D.P., Hall, A.M. 2008. Modelling the processes of cliff-top erosion and deposition under extreme storm waves. *Marine Geology*, 253, 36–50. https://doi.org/10.1016/j.margeo.2008.02.015

Harley, M. 2017. Coastal Storm Definition, in: Ciavola P., Coco G. (Eds.), Coastal Storms: Processes and Impacts, John Wiley & Sons Inc. https://doi.org/10.1002/9781118937099.ch1

Jaud, M., Delacourt, C., Le Dantec, N., Allemand, P., Ammann, J., Grandjean, P., Nouaille, H., Prunier, C., Cuq, V., Augereau, E., Cocquempot, L., Floc'h, F. 2019. Diachronic UAV photogrammetry of a sandy beach in Brittany (France) for a long-term coastal observatory. *ISPRS International Journal of Geo-Information*, 8(6), 267. https://doi.org/10.3390/ijgi8060267

Jóhannesson, H. 1989. Aldur Hallmundarhrauns í Borgarfirdi (Age of the Hallmundarhraun lava flow, Reykjanes peninsula, SW-Iceland). *Fjölrit Náttútufraedistofnunar*, 9, 13 p. https://utgafa.ni.is/fjolrit/Fjolrit_09.pdf

Jóhannesson, H., Einarsson, S. 1988a. Aldur Illahrauns við Svartsengi (Age of the Illahraun lava flow, Reykjanes peninsula, SW-Iceland). *Fjölrit Náttútufraedistofnunar*, 7, 10 p. https://utgafa.ni.is/fjolrit/Fjolrit_07.pdf

Jóhannesson, H., Einarsson, S. 1988b. Krísuvíkureldar. I. Aldur Ögmundarhrauns og midaldalagsins (The Krísuvík fires. I. Age of the Ögmundarhraun lava and the Medieval tephra layer). *Jökull,* 38, 71–87.

Jónsson, J. 1983. Eldgos á sögulegum timá á Reykjanesskaga (Volcanic eruptions in historical time on the Reykjanes peninsula, South-West Iceland). *Náttúrufraedingurinn*, 52, 127–139.

Kennedy, A.B., Cox, R., Dias, F. 2021. Storm Waves May Be the Source of Some "Tsunami" Coastal Boulder Deposits. *Geophysical Research Letters,* 48, e2020GL090775. https://doi.org/10.1029/2020GL090775

Kennedy, A.B., Mori, N., Zhang, Y., Yasuda, T., Chen, S., Tajima, Y., Pecor, W., Toride, K. 2016. Observations and modeling of coastal boulder transport and loading during super typhoon Haiyan. *Coastal Engineering Journal,* 58(1), 1640004-1–1640004-25. https://doi.org/10.1142/S0578563416400040

Kennedy, A.B., Mori, N., Yasuda, T., Shimozono, T., Tomiczek, T., Donahue, A., Shimura, T., Imai, Y. 2017. Extreme block and boulder transport along a cliffed coastline (Calicoan Island, Philippines) during Super Typhoon Haiyan. *Marine Geology,* 383, 65–77. https://doi.org/10.1016/j.margeo.2016.11.004

Kennedy, D.M., Woods, J.L.D., Naylor, L.A., Hansom, J.D., Rosser, N.J. 2019. Intertidal boulder-based wave hindcasting can underestimate wave size: Evidence from Yorkshire, UK. *Marine Geology*, 411, 98–106. https://doi.org/10.1016/j.margeo.2019.02.002

Larusson, E. 2010. Iceland, in Bird, E.C.F. (Eds.), Encyclopedia of the World's Coastal Landforms, Springer Netherlands, Dordrecht, pp. 323–332.

Lau, A.Y.A., Autret, R. 2020. Spatial patterns of subaerial coarse clasts, in: Engel, M., Pilarczyk, J., May, S.M., Brill, D., Garrett, E.d. (Eds.), Geological Records of Tsunamis and Other Extreme Waves, Elsevier, pp. 513–546.

Lau, A.Y.A., Terry, J.P., Ziegler, A.D., Switzer, A.D., Lee, Y., Etienne, S. 2016. Understanding the history of extreme wave events in the Tuamotu Archipelago of French Polynesia from large carbonate boulders on Makemo Atoll, with implications for future threats in the central South Pacific. *Marine Geology*, 380, 174–190. https://doi.org/10.1016/j.margeo.2016.04.018

Lorang, M.S. 2011. A wave-competence approach to distinguish between boulder and megaclast deposits due to storm waves versus tsunamis. *Marine Geology,* 283, 90–97. https://doi.org/10.1016/j.margeo.2010.10.005

Marie, G. 2007. Les conséquences morphologiques des tempêtes et tsunamis sur les littoraux volcaniques de l'île d'Hawaï (Big Island) : genèse de plates-formes de haute mer et dépôts de blocs, in: Etienne S., Paris R. (Eds.), Les littoraux volcaniques: une approche environnementale. Edit. Presses Universitaires Blaise-Pascal, Clermont-Ferrand, pp. 101–119.

Masselink, G., Castelle, B., Scott, T., Dodet, G., Suanez, S., Jackson, D., Floc'h, F. 2016. Extreme wave activity during 2013/2014 winter and morphological impacts along the Atlantic coast of Europe. *Geophysical Research Letters*, 43, 2015GL067492. https://doi.org/10.1002/2015GL067492

Masselink, G., Scott, T., Poate, T., Russell, P., Davidson, M., Conley, D. 2015. The extreme 2013/2014 winter storms: hydrodynamic forcing and coastal response along the southwest coast of England. *Earth Surface Processes and Landforms*, 41(3), 378-391, https://doi.org/10.1002/esp.3836

Matthews, N.A. 2008. Aerial and close-range photogrammetric technology: providing resource documentation, interpretation, and preservation. US Bureau of Land Management: Washington, D.C. 53 p. https://www.blm.gov/sites/default/files/documents/files/Library_BLMTechnicalNote428_0.pdf

May, S.M., Engel, M., Brill, D., Cuadra, C., Lagmay, A.M.F., Santiago, J., Suarez, J.K., Reyes, M., Brückner, H. 2015. Block and boulder transport in Eastern Samar (Philippines) during Supertyphoon Haiyan. *Earth Surface Dynamics*, 3, 543–558. https://doi.org/10.5194/esurf-3-543-2015

McKenna, J. 1990. Morphodynamics and sediments of basalt shore platforms. PhD Thesis, University of Ulster.

Mhammdi, N., Medina, F., Belkhayat, Z., El Aoula, R., Geawahri, M.-A., Chiguer, A. 2019. Marine storms along the Moroccan Atlantic coast: an underrated natural hazard? *Journal of African Earth Sciences*, 163, 103730. https://doi.org/10.1016/j.jafrearsci.2019.103730

Mosbrucker, A.R., Major, J.J., Spicer, K.R., Pitlick, J. 2017. Camera system considerations for geomorphic applications of SfM photogrammetry. *Earth Surface Processes and Landforms*, 42, 969–986. https://doi.org/10.1002/esp.4066

Nagle-McNaughton, T., Cox, R. 2020. Measuring Change Using Quantitative Differencing of Repeat Structure-From-Motion Photogrammetry: The Effect of Storms on Coastal Boulder Deposits. *Remote Sensing*, 12, https://doi.org/10.3390/rs12010042

Nanayama F, Shigeno K, Satake K, Shimokawa K, Koitabashi S, Miyasaka S, Ishii M. 2000. Sedimentary differences between the 1993 Hokkaido-nansei-oki tsunami and the 1959 Miyakojima typhoon at Taisei, southwestern Hokkaido, northern Japan. *Sedimentary Geology*, 135, 255–264. https://doi.org/10.1016/S0037-0738(00)00076-2

Naylor, L.A., Stephenson, W.J. 2010. On the role of discontinuities in mediating shore platform erosion. *Geomorphology*, 114(1-2), 89–100. https://doi.org/10.1016/j.geomorph.2008.12.024

Naylor, L.A., Stephenson, W.J., Smith, H.C.M., Way O., Mendelssohn J., Cowley A. 2016. Geomorphological control on boulder transport and coastal erosion before, during and after an extreme extra-tropical cyclone. *Earth Surface Processes and Landforms*, 41, 685–700. https://doi.org/10.1002/esp.3900

Nelsen, R.B. 2006. An Introduction to Copulas. Springer New York, New York.

Nicolae Lerma, A., Castelle, B., Marieu, V., Robinet, A., Bulteau, T., Bernon, N., Mallet, C. 2022. Decadal beach-dune profile monitoring along a 230-km high-energy sandy coast: Aquitaine, southwest France. *Applied Geography,* 139, 102645. https://doi.org/10.1016/j.apgeog.2022.102645

Nott, J., 2003. Tsunami or storm waves? — determining the origin of a spectacular field of wave emplaced boulders using numerical storm surge and wave models and hydrodynamic transport equations. *Journal of Coastal Research*, 19(2), 348–356. https://www.jstor.org/stable/4299176

Oliveira, M.A., Llop, E., de Andrade, C.F., Branquinho, C., Goble, R., Queiroz, S., Freitas, M.C., Pinho, P. 2020a. Estimating the age and mechanism of boulder transport related with extreme waves using lichenometry. *Progress in Physical Geography: Earth and Environment*, 44(6), 870–897. https://doi.org/10.1177/0309133320927629

Oliveira, M.A., Scotto, M.G., Barbosa, S., de Andrade, C.F., Freitas, M. da C. 2020b. Morphological controls and statistical modelling of boulder transport by extreme storms. *Marine Geology*, 426, 106216. DOI: 10.1016/j.margeo.2020.106216

Paris, R., Naylor, L.A., Stephenson, W.J. 2011. Boulders as a signature of storms on rock coasts. *Marine Geology*, 283, 1–11. https://doi.org/10.1016/j.margeo.2011.03.016

Pawlowicz, R., Beardsley, B., Lentz, S. 2002. Classical tidal harmonic analysis including error estimates in MATLAB using T_TIDE. *Computers & Geosciences,* 28, 929–937. https://doi.org/10.1016/S0098-3004(02)00013-4

Pepe, F., Corradino, M., Parrino, N., Besio, G., Presti, V.L., Renda, P., Calcagnile, L., Quarta, G., Sulli, A., Antonioli, F. 2018. Boulder coastal deposits at Favignana Island rocky coast (Sicily, Italy): Litho-structural and hydrodynamic control. *Geomorphology*, 303, 191–209. https://doi.org/10.1016/j.geomorph.2017.11.017

Piscitelli, A., Milella, M., Hippolyte, J.-C., Shah-Hosseini, M., Morhange, C., Mastronuzzi, G. 2017. Numerical approach to the study of coastal boulders: The case of Martigues, Marseille, France. *Quaternary International*, 439, 52–64. https://doi.org/10.1016/j.quaint.2016.10.042

Prizomwala, S.P., Gandhi, D., Ukey, V.M., Bhatt, N., Rastogi, B.K. 2015. Coastal boulders as evidences of high-energy marine events from Diu Island, west coast of India: storm or palaeotsunami? *Natural Hazards*, 75, 1187–1203. https://doi.org/10.1007/s11069-014-1371-5

Ramalho, R.S., Quartau, R., Trenhaile, A.S., Mitchell, N.C., Woodroffe, C.D., Ávila, S.P. 2013. Coastal evolution on volcanic oceanic islands: A complex interplay between volcanism, erosion, sedimentation, sea-level change and biogenic production. *Earth-Science Reviews*, 127, 140–170. https://doi.org/10.1016/j.earscirev.2013.10.007

Richmond, B.M., Buckley, M., Etienne, S., Chagué-Goff, C., Clark, K., Goff, J., Dominey-Howes, D., Strotz, L. 2011a. Deposits, flow characteristics, and landscape change resulting from the September 2009 South Pacific tsunami in the Samoan islands. *Earth-Science Reviews*, 107, 38–51. https://doi.org/10.1016/j.earscirev.2011.03.008

Richmond, B.M., Watt, S., Buckley, M., Jaffe, B.E., Gelfenbaum, G., Morton, R.A. 2011b. Recent storm and tsunami coarse-clast deposit characteristics, southeast Hawai‘i. *Marine Geology*, 283, 79–89. https://doi.org/10.1016/j.margeo.2010.08.001

Sadegh, M., Moftakhari, H., Gupta, H.V., Ragno, E., Mazdiyasni, O., Sanders, B., Matthew, R., AghaKouchak, A. 2018. Multihazard scenarios for analysis of compound extreme events. *Geophysical Research Letters*, 45, 5470–5480. https://doi.org/10.1029/2018GL077317

Sæmundsson, K., Sigurgeirsson, M.Á., Hjartarson, Á., Kaldal, I., Kristinsson, S.G. 2016. Geological Map of of Southweast Iceland (2nd edit.), Southern Part. 1:100.000. Reykjavík, Iceland GeoSurvey and Landsvirkjun.

Saintilan, N., Rogers, K. 2005. Recent Storm Boulder Deposits on the Beecroft Peninsula, New South Wales, Australia. *Geographical Research,* 43(4), 429–432. https://doi-org.scd-proxy.univ-brest.fr/10.1111/j.1745-5871.2005.00344.x

Salzmann, L., Green, A. 2012. Boulder emplacement on a tectonically stable, wave-dominated coastline, Mission Rocks, northern KwaZulu-Natal, South Africa. Marine Geology, 323–325, 95–106. https://doi.org/10.1016/j.margeo.2012.07.001

Scicchitano, G., Scardino, G., Tarascio, S., Monaco, C., Barracane, G., Locuratolo, G., Milella, M., Piscitelli, A., Mazza, G., Mastronuzzi, G. 2020. The First Video Witness of Coastal Boulder Displacements Recorded during the Impact of Medicane “Zorbas” on Southeastern Sicily. *Water*, 12, 1497. https://doi.org/10.3390/w12051497

Schinke, H., 1993. On the occurrence of deep cyclones over Europe and the North Atlantic in the period 1930– 1991. *Beitrage zur Physik der Atmosphare*, 66, 223–237.

Shah-Hosseini, M., Saleem, A., Mahmoud, A.-M.A., Morhange, C. 2016. Coastal boulder deposits attesting to large wave impacts on the Mediterranean coast of Egypt. *Natural Hazards*, 83, 849–865. https://doi.org/10.1007/s11069-016-2349-2

Shelley, D. 1968. Fitting boulders: the result of an important shore process. *Nature,* 220, 1020–1021. https://doi.org/10.1038/2201020a0

Sigbjarnarson, G., 1986. *The wave climate in Iceland*. Iceland Coastal and River Symposium, Proceedings. University of Iceland, Icelandic Harbour Authority and National Energy Authority, Reykjavik.

Soria, J.L.A., Switzer, A.D., Pilarczyk, J.E., Tang, H., Weiss, R., Siringan, F., Manglicmot, M., Gallentes, A., Lau, A.Y.A., Yee Lin Cheong, A., Wei Ling Koh, T. 2018. Surf beat-induced overwash during Typhoon Haiyan deposited two distinct sediment assemblages on the carbonate coast of Hernani, Samar, central Philippines. *Marine Geology,* 396, 215–230. https://doi.org/10.1016/j.margeo.2017.08.016.

Spiske, M., Bahlburg, H. 2011. A quasi-experimental setting of coarse clast transport by the 2010 Chile tsunami (Bucalemu, Central Chile). *Marine Geology*, 289, 72–85. https://doi.org/10.1016/j.margeo.2011.09.007

Spiske, M., Tang, H., Bahlburg, H. 2019. Post-depositional alteration of onshore tsunami deposits – Implications for the reconstruction of past events. Earth-Science Reviews : 103068. https://doi.org/10.1016/j.earscirev.2019.103068

Suanez S, Fichaut B, Magne R. 2009. Cliff-top storm deposits on Banneg Island, Brittany, France: Effects of giant waves in the Eastern Atlantic Ocean. *Sedimentary Geology*, 220, 12–28. https://doi.org/10.1016/j.sedgeo.2009.06.004

Sussmilch C.A. 1912. Notes on some recent marine erosion at Bondi. Journal and Proceedings of the Royal Society of New South Wales, 46, 155–158.

Swirad, Z.M., Rosser, N.J., Brain, M.J. 2019. Identifying mechanisms of shore platform erosion using Structure-from-Motion (SfM) photogrammetry. *Earth Surface Processes and Landforms*, 44, 1542–1558. https://doi.org/10.1002/esp.4591

Switzer A.D., Burston J.M. 2010. Competing mechanisms for boulder deposition on the southeast Australian coast. Geomorphology, 114(1–2), 42–54. https://doi.org/10.1016/j.geomorph.2009.02.009.

Terry, J.P., Dunne, K., Jankaew, K. 2016. Prehistorical frequency of high-energy marine inundation events driven by typhoons in the Bay of Bangkok (Thailand), interpreted from coastal carbonate boulders. Earth Surface Processes and Landforms, 41, 553–562. https://doi.org/10.1002/esp.3873

Tomasson, G., Gislason, K., Karlsson, T. 1997. A storm surge model for the coast of Iceland. *WIT Transactions on The Built Environment*, 27, 85–94. https://www.witpress.com/Secure/elibrary/papers/CE97/CE97009FU.pdf

Torres-Sánchez, J., López-Granados, F., Borra-Serrano, I., Peña, J.M. 2018. Assessing UAV-collected image overlap influence on computation time and digital surface model accuracy in olive orchards. *Precision Agriculture*, 19, 115–133. https://doi.org/10.1007/s11119-017-9502-0

Turner, I.L., Harley, M.D., Short, A.D., Simmons, J.A., Bracs, M.A., Phillips, M.S., Splinter, K.D. 2016. A multi-decade dataset of monthly beach profile surveys and inshore wave forcing at Narrabeen, Australia. *Scientific Data*, 3, https://doi.org/10.1038/sdata.2016.24

Viggósson, G., Elíasson, J., Sigurðarson, S. 2016. Ákvörðun á flóðhæð í Básendaflóði. Áfangaskýrsla. Vegagerðin, Reykjavík.

Watanabe, M., Goto, K., Imamura, F., Kennedy, A., Sugawara., D, Nakamura, N., Tonosaki, T. 2019. Modeling boulder transport by coastal waves on cliff topography: Case study at Hachijo Island, Japan. *Earth Surface Processes and Landforms*, 44, 2939–2956. https://doi.org/10.1002/esp.4684

Weiss, R., Sheremet, A. 2017. Toward a new paradigm for boulder dislodgement during storms: new paradigm for boulder dislodgement. *Geochemistry, Geophysics, Geosystems*, 18, 2717–2726. https://doi.org/10.1002/2017GC006926

Westoby M.J., Brasington, J., Glasser, N.F., Hambrey, M.J., Reynolds, J.M. 2012. 'Structure-from-Motion' photogrammetry: A low-cost, effective tool for geoscience applications. *Geomorphology*, 179, 300–314. https://doi.org/10.1016/j.geomorph.2012.08.021

Wheaton, J.M., Brasington, J., Darby, S.E., Sear, D.A. 2009. Accounting for uncertainty in DEMs from repeat topographic surveys: improved sediment budgets. *Earth Surface Processes and Landforms*, 35, 136–156. https://doi.org/10.1002/esp.1886

Williams, D.M., Hall, A.M. 2004. Cliff-top megaclast deposits of Ireland, a record of extreme waves in the North Atlantic—storms or tsunamis? *Marine Geology*, 206(1–4), 101–117. https://doi.org/10.1016/j.margeo.2004.02.002

Zainali, A., Weiss, R. 2015. Boulder dislodgement and transport by solitary waves: Insights from three-dimensional numerical simulations: 3D simulation of boulder transport. *Geophysical Research Letters*, 42, 4490–4497. https://doi.org/10.1002/2015GL063712

Zhang, W., Qi J., Wan, P., Wang, H., Xie, D., Wang, X., Yan, G. 2016. An Easy-to-Use Airborne LiDAR Data Filtering Method Based on Cloth Simulation. *Remote Sensing*, 8, 501. https://doi.org/10.3390/rs8060501

Figure01

Click here to access/download;Figure;Figure01_Autret-et-al.tif

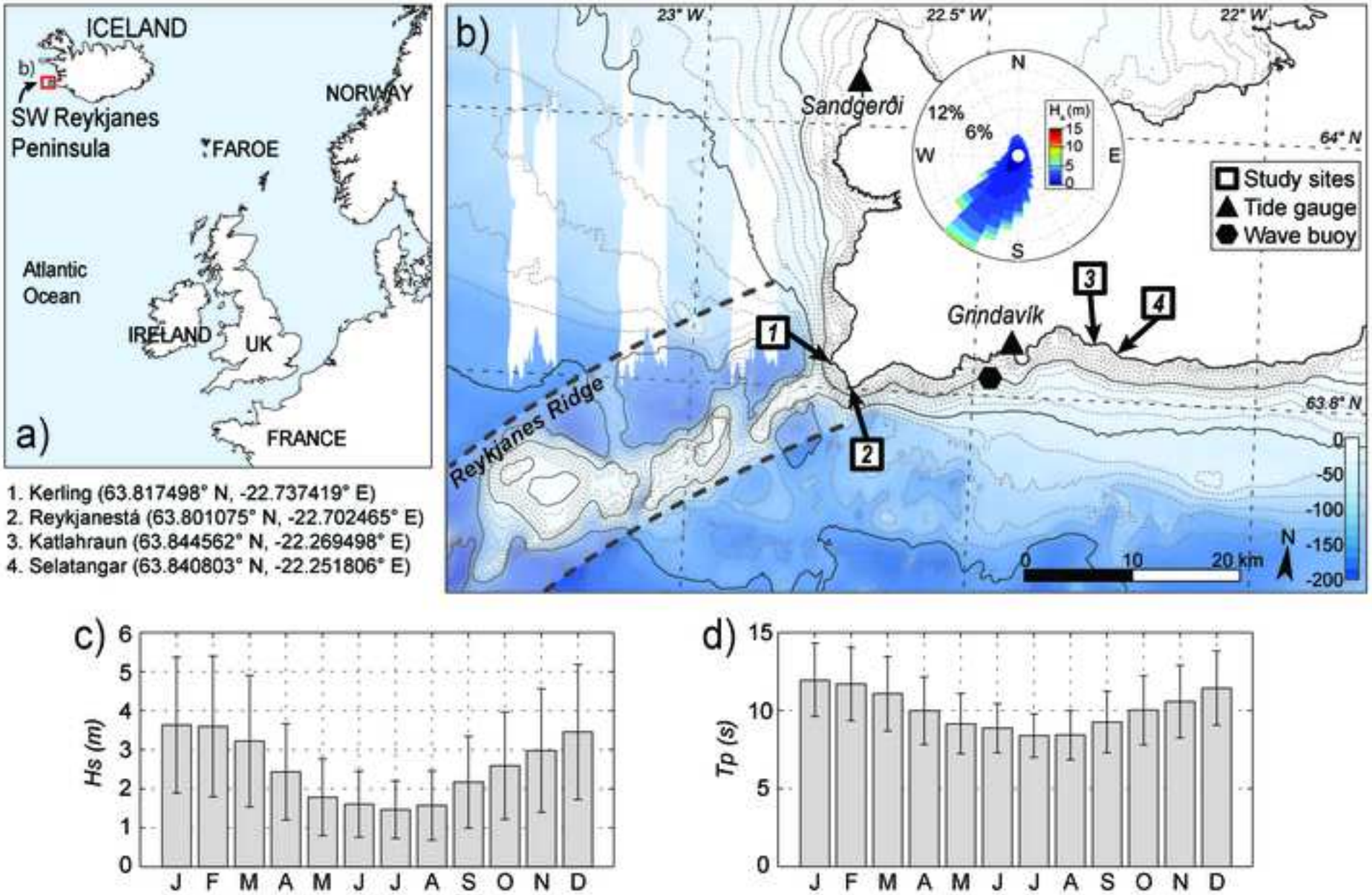

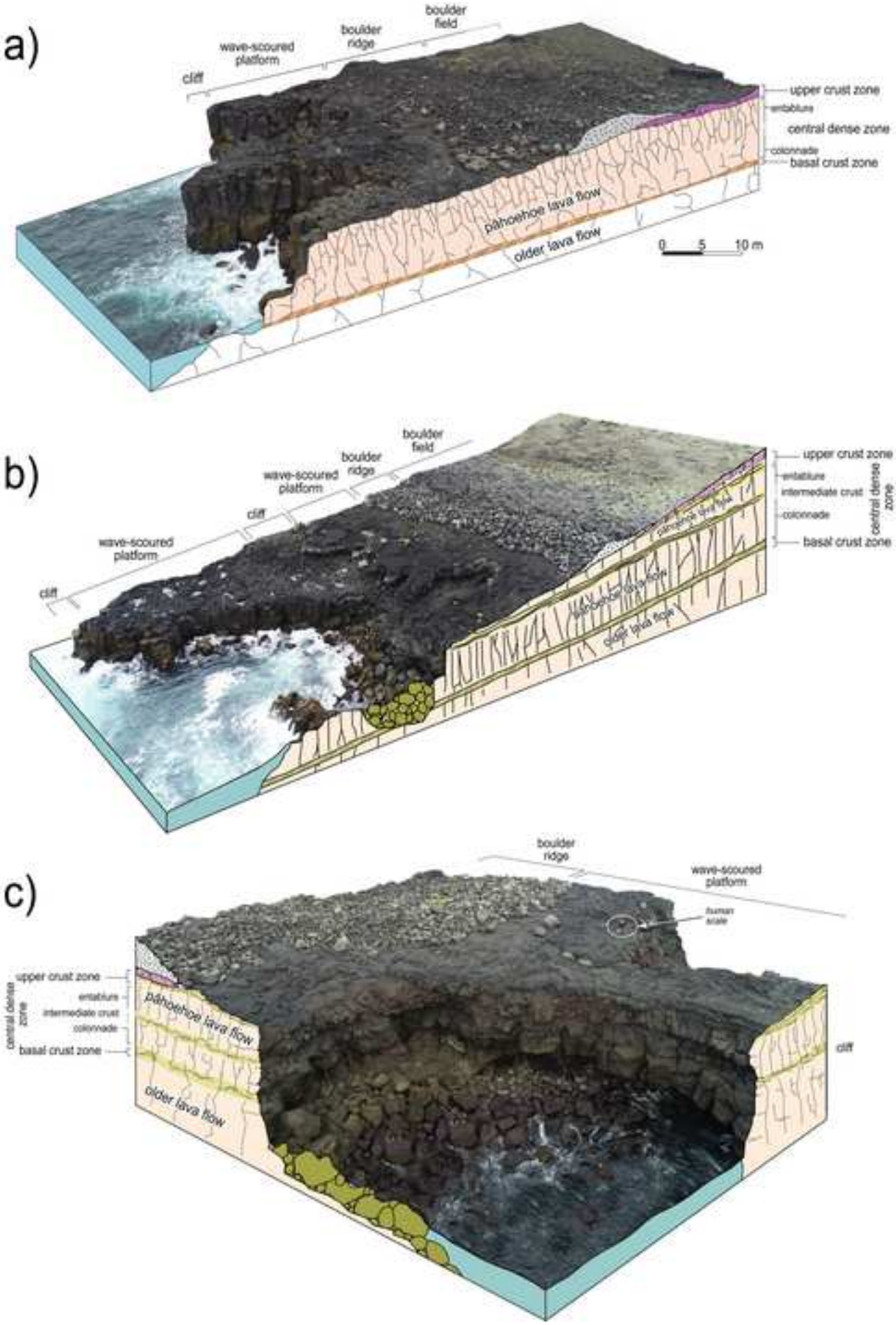
a)
boulder field
boulder ridge
wave-scoured platform
cliff
upper crust zone
entablure
central dense zone
colonnade
basal crust zone
pahoehoe lava flow
older lava flow
0 5 10 m
b)
boulder field
boulder ridge
wave-scoured platform
cliff
wave-scoured platform
cliff
upper crust zone
entablure
intermediate crust
colonnade
central dense zone
basal crust zone
older lava flow
c)
boulder ridge
wave-scoured platform
human scale
upper crust zone
entablure
intermediate crust
colonnade
central dense zone
basal crust zone
pahoehoe lava flow
older lava flow
cliff

Figure03a

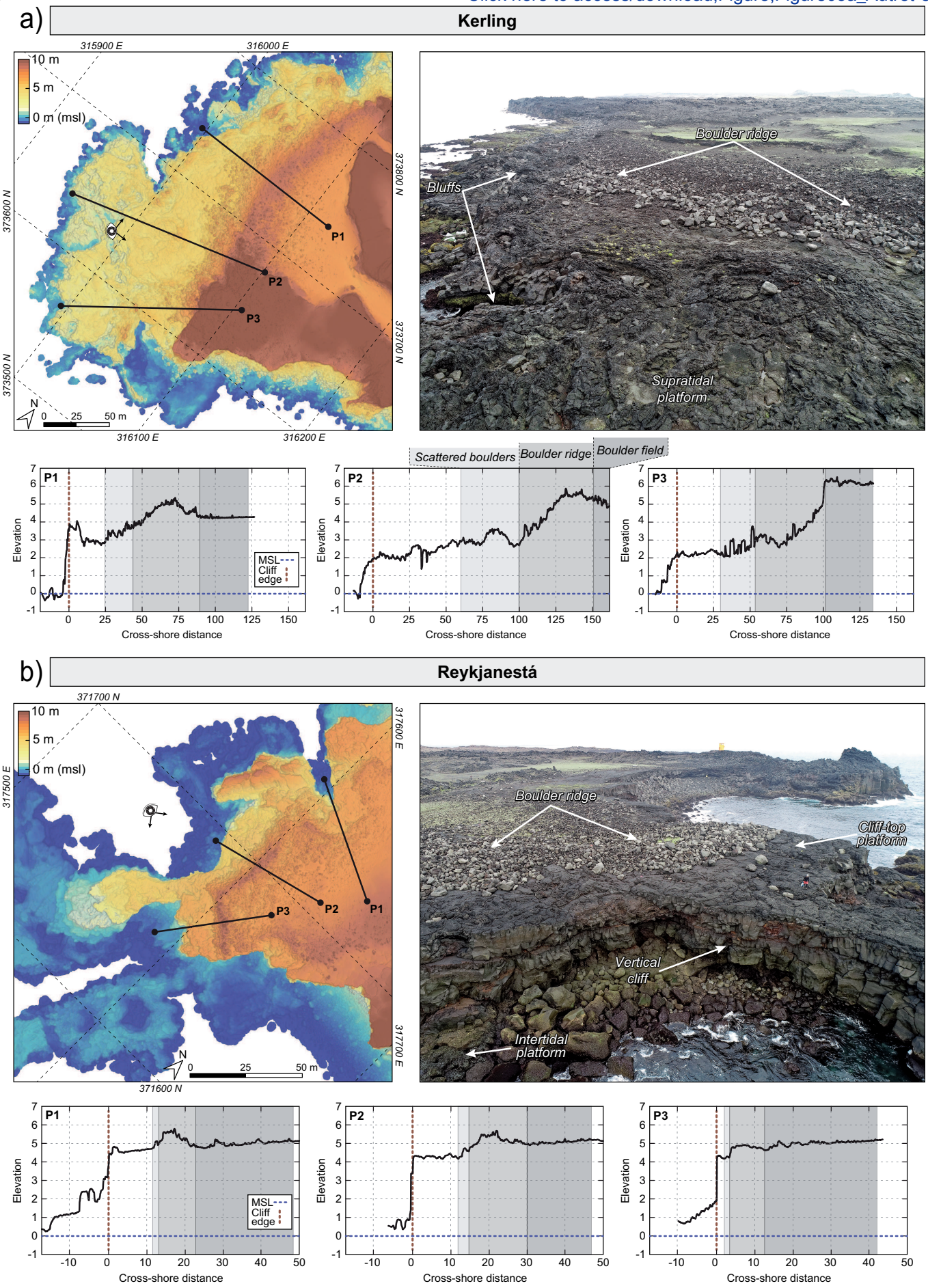

Figure03b

Click here to access/download;Figure;Figure03b_Autret-et-al.tif

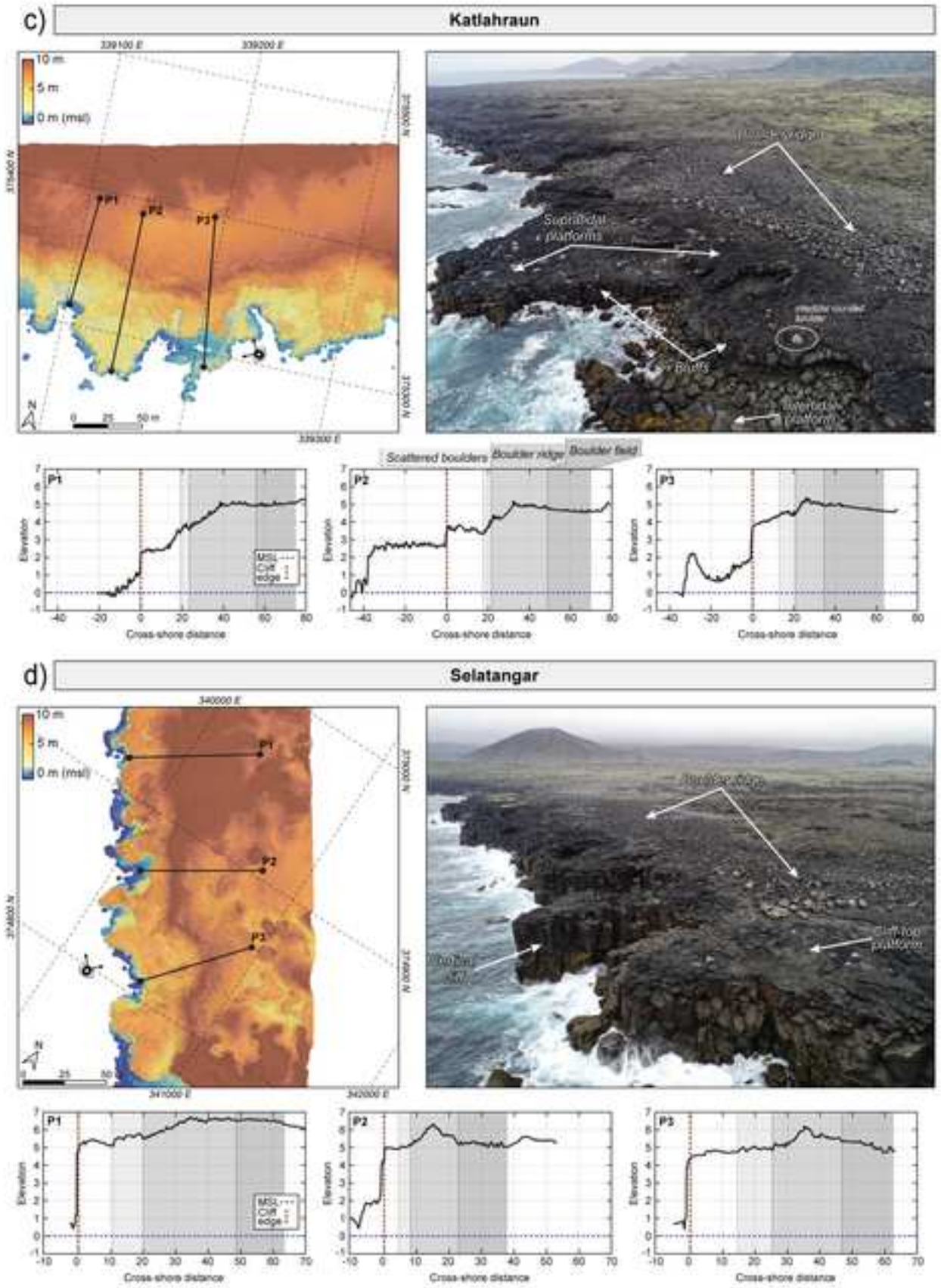

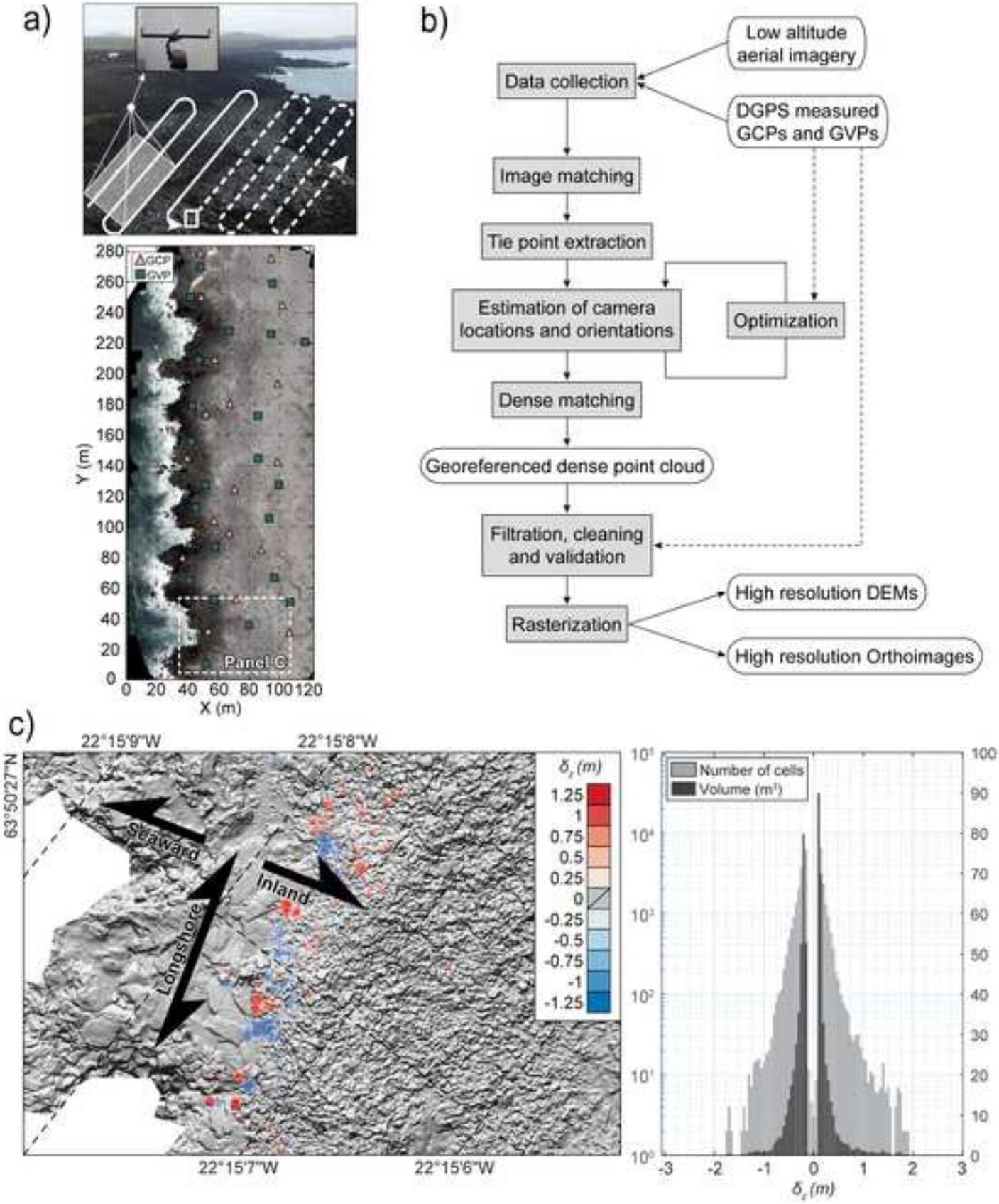
a)
GCP
GVP
Y (m)
X (m)
Panel C
b)
Low altitude aerial imagery
Data collection
DGPS measured GCPs and GVPs
Image matching
Tie point extraction
Estimation of camera locations and orientations
Optimization
Dense matching
Georeferenced dense point cloud
Filtration, cleaning and validation
Rasterization
High resolution DEMs
High resolution Orthoimages
c)
22°15'9"W
22°15'8"W
63°50'27"N
Seaward
Inland
Longshore
22°15'7"W
22°15'6"W
δz (m)
Number of cells
Volume (m³)
δz (m)

Figure05

Click here to access/download;Figure;Figure05_Autret-et-al.tif

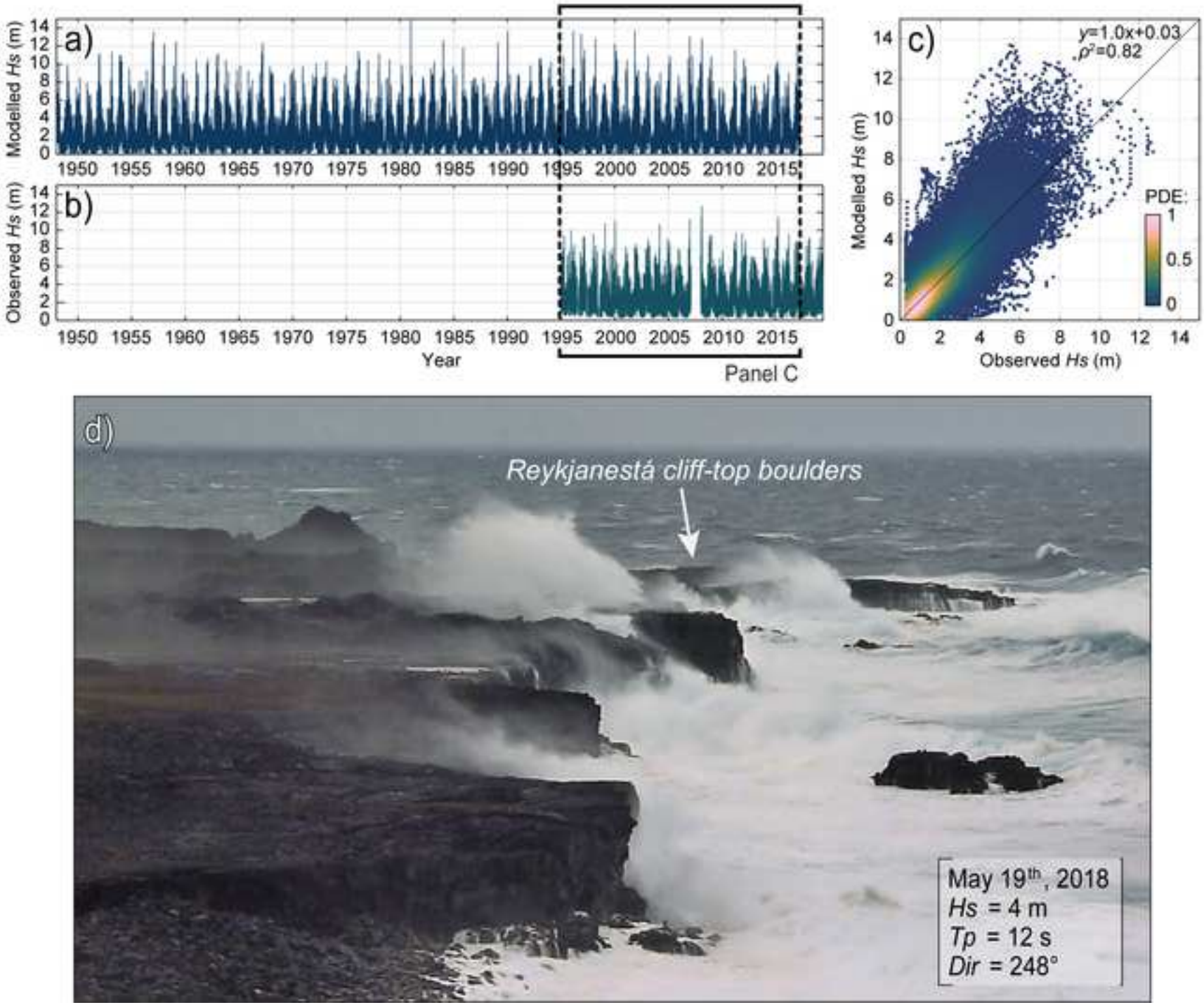

Figure06

Click here to access/download;Figure;Figure06_Autret-et-al.tif

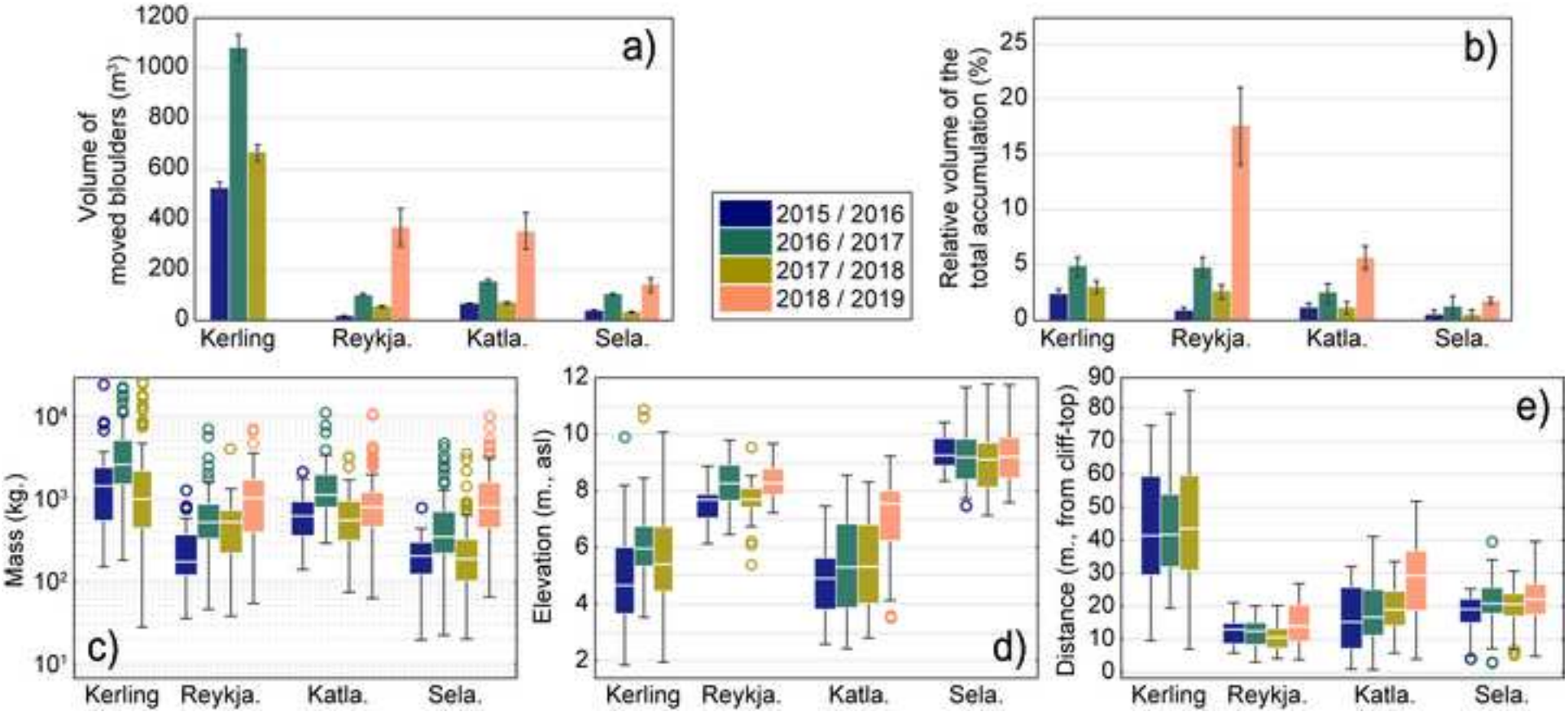

Figure07

Click here to access/download;Figure;Figure07_Autret-et-al.tif

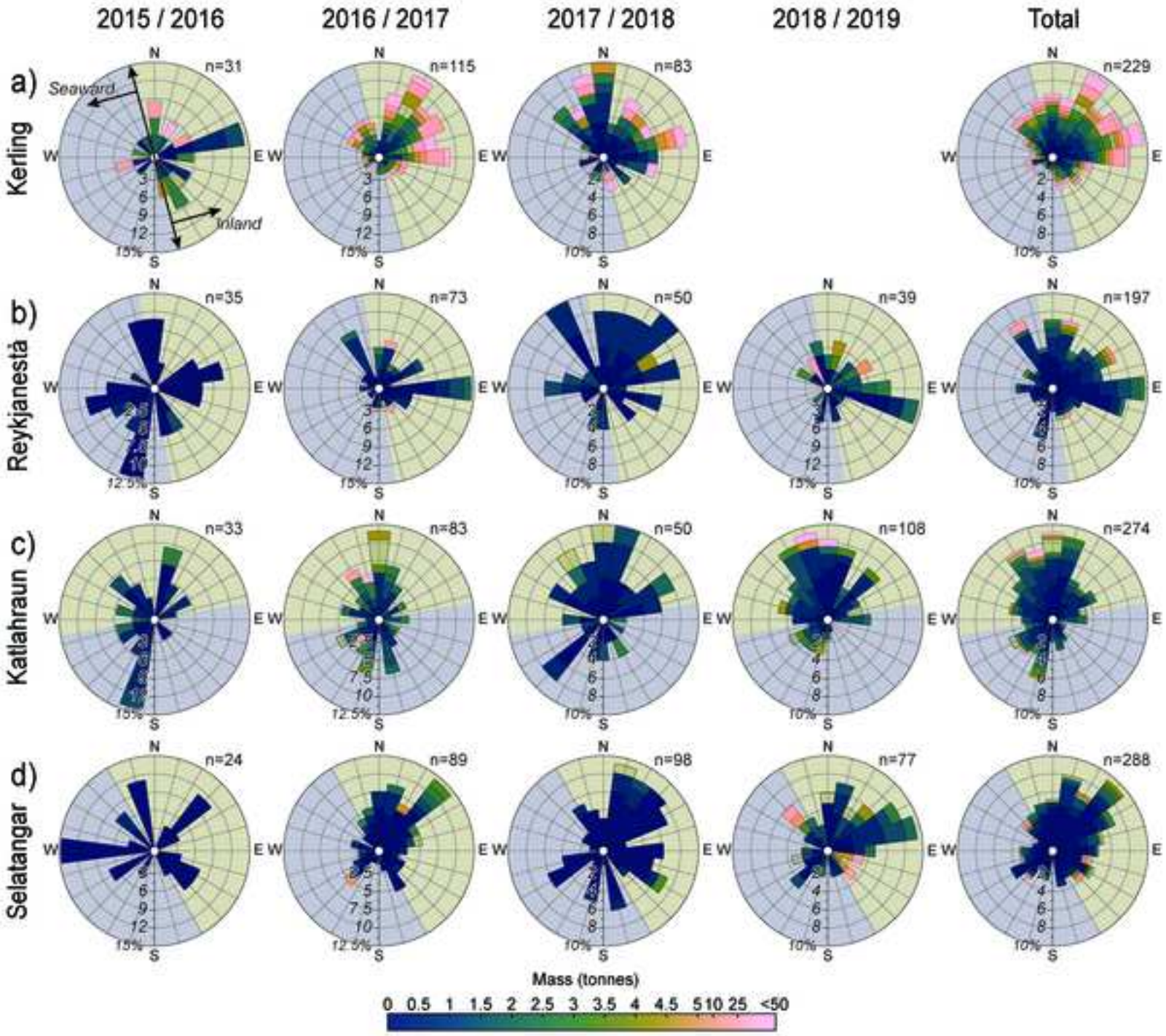

Figure08

Click here to access/download;Figure;Figure08_Autret-et-al.tif

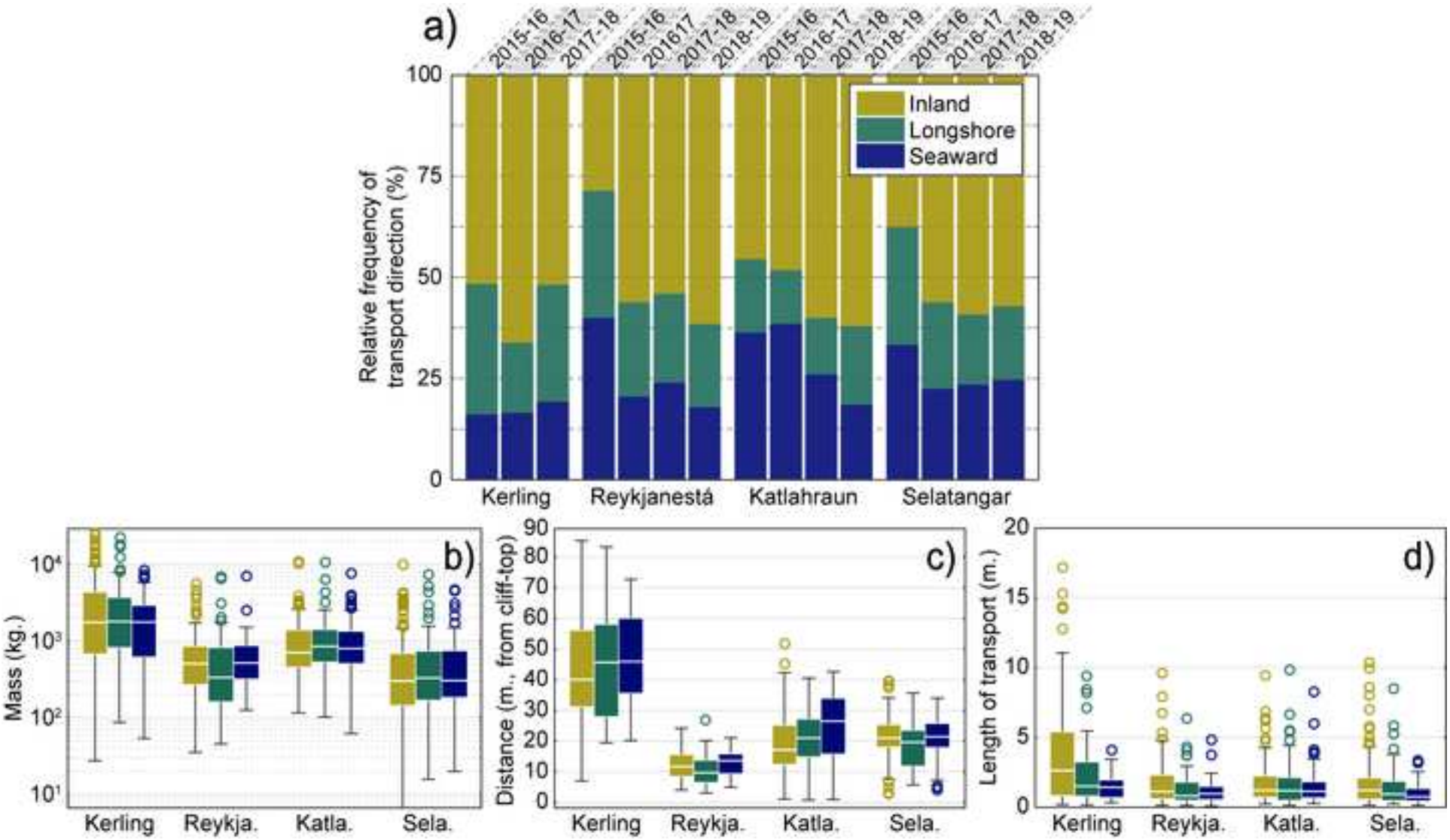

Figure09 Click here to access/download;Figure;Figure09_Autret-et-al.tif

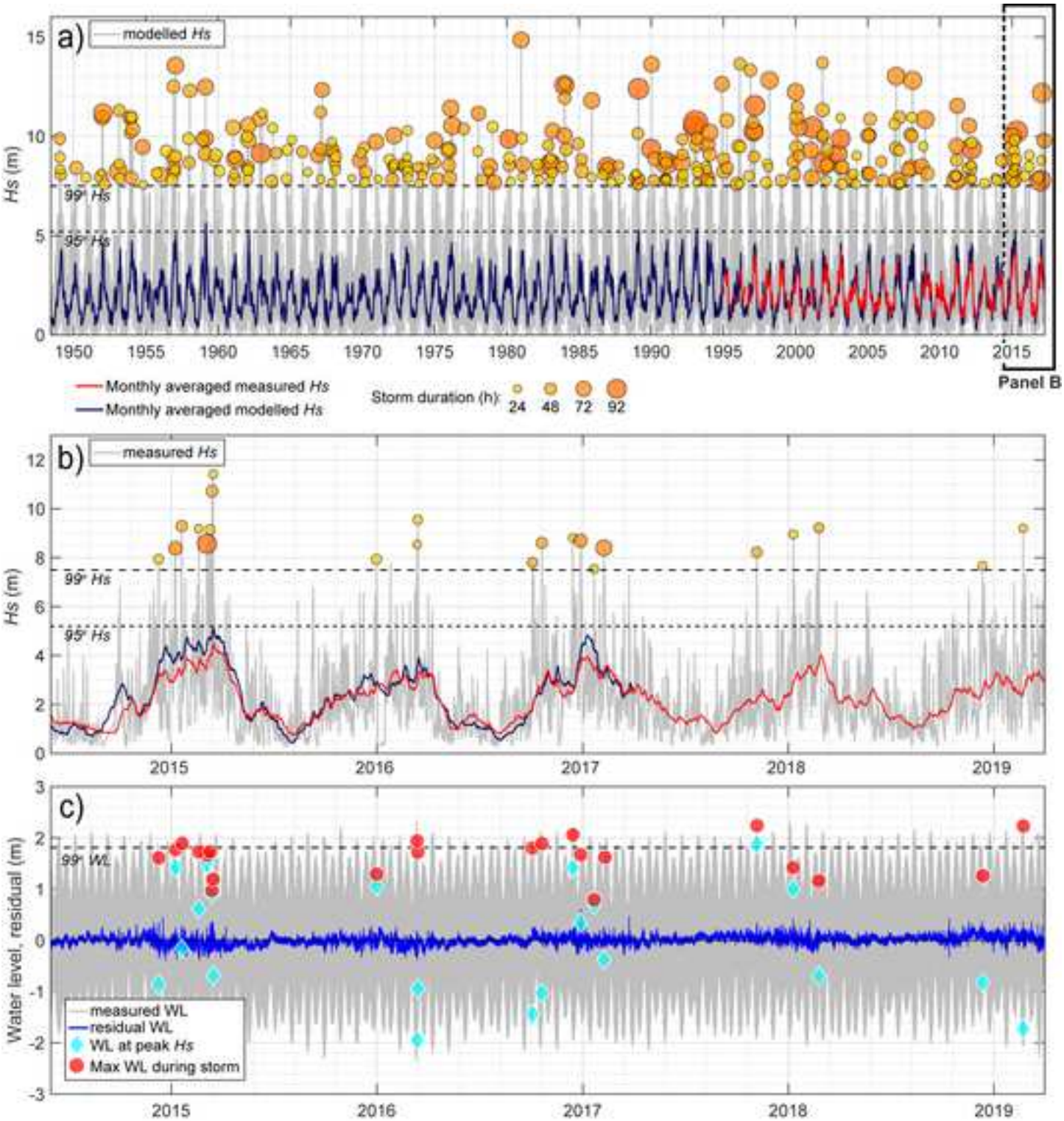

Figure10

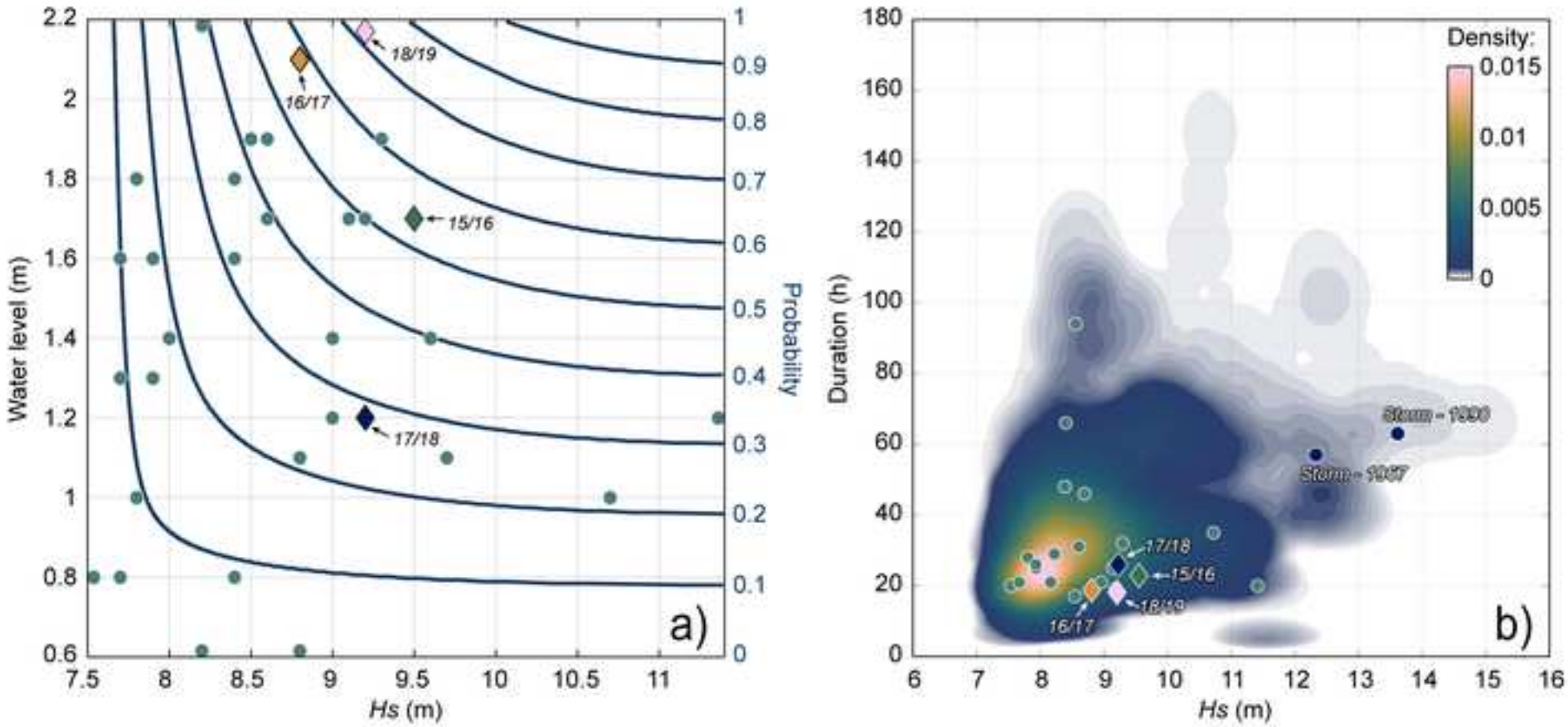

Figure11 Click here to access/download;Figure;Figure11_Autret-et-al.tif

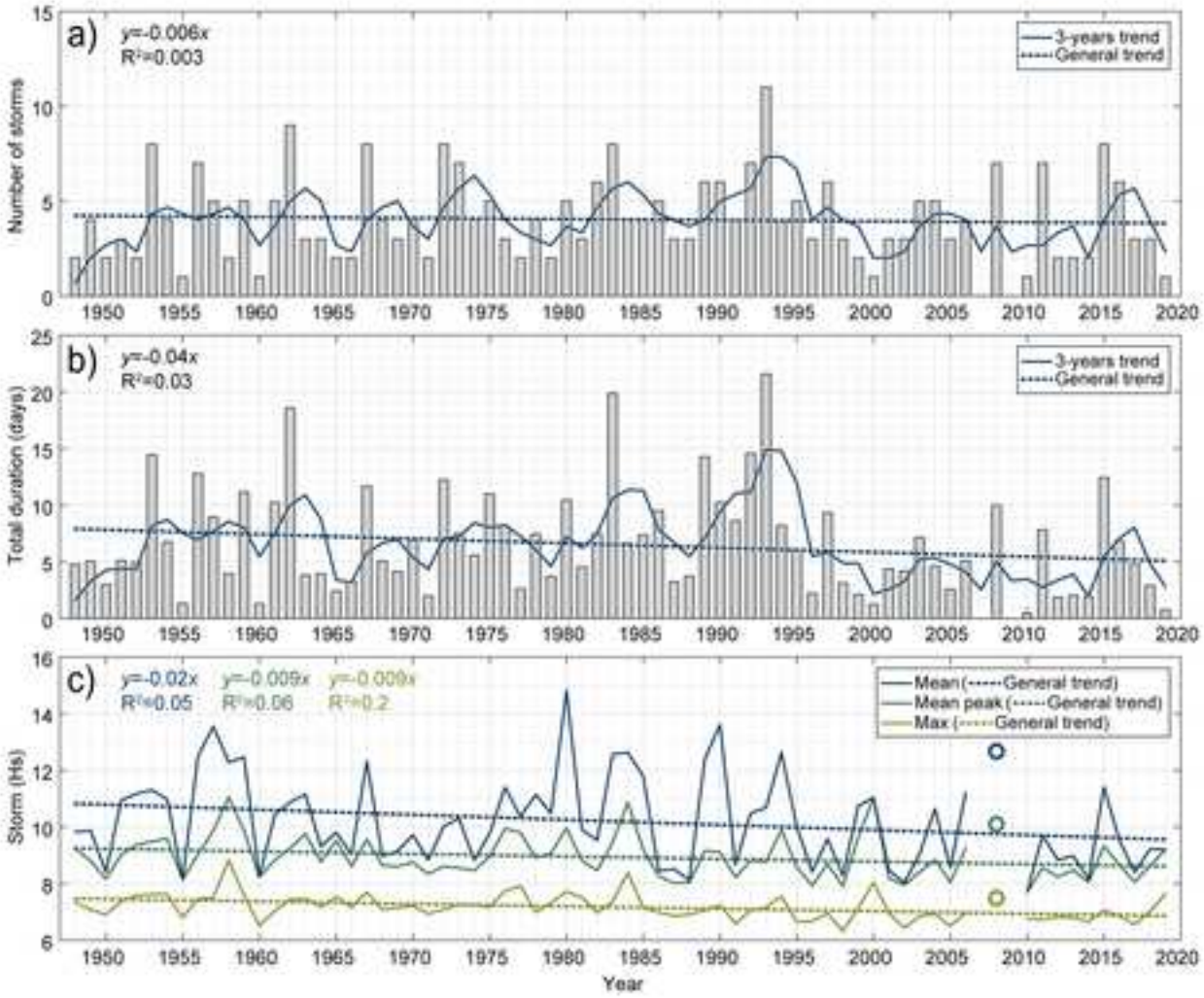

Figure12

Click here to access/download;Figure;Figure12_Autret-et-al.tif

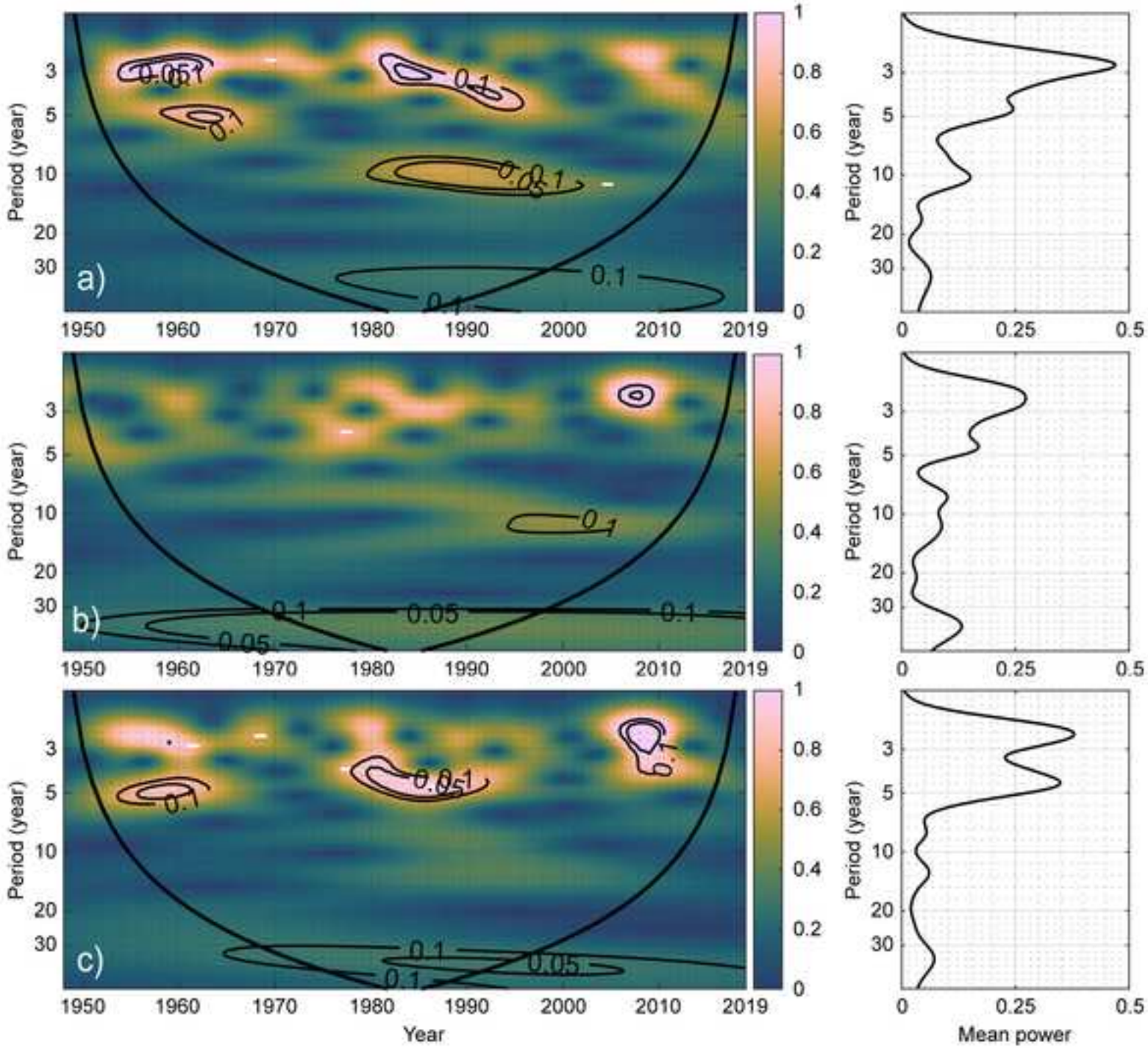

Figure13